

Mass Loss from the Exoplanet WASP-12b Inferred from *Spitzer* Phase Curves

Taylor J. Bell,^{1,2}★ Michael Zhang,³ Patricio E. Cubillos,⁴ Lisa Dang,^{1,2} Luca Fossati,⁴ Kamen O. Todorov,⁵ Nicolas B. Cowan,^{1,2,6} Drake Deming,⁷ Robert T. Zellem,⁸ Kevin B. Stevenson,⁹ Ian J. M. Crossfield,¹⁰ Ian Dobbs-Dixon,¹¹ Jonathan J. Fortney,¹² Heather A. Knutson,¹³ and Michael R. Line¹⁴

¹Department of Physics, McGill University, 3600 rue University, Montréal, QC H3A 2T8, Canada

²McGill Space Institute; Institute for Research on Exoplanets; Centre for Research in Astrophysics of Quebec

³Department of Astronomy, California Institute of Technology, 1216 E California Blvd, Pasadena, CA 91125, USA

⁴Space Research Institute, Austrian Academy of Sciences, Schmiedlstrasse 6, A-8042 Graz, Austria

⁵Anton Pannekoek Institute for Astronomy, University of Amsterdam, Science Park 904, 1090 GE Amsterdam, The Netherlands

⁶Department of Earth & Planetary Sciences, McGill University, 3450 rue University, Montréal, QC H3A 0E8, Canada

⁷Department of Astronomy, University of Maryland, College Park, MD 20742, USA

⁸Jet Propulsion Laboratory, California Institute of Technology, 4800 Oak Grove Drive, Pasadena, CA 91109, USA

⁹Space Telescope Science Institute, Baltimore, MD 21218, USA

¹⁰Department of Physics, Massachusetts Institute of Technology, Cambridge, MA, USA

¹¹Department of Physics, NYU Abu Dhabi, P.O. Box 129188, Abu Dhabi, UAE

¹²Other Worlds Laboratory, Department of Astronomy and Astrophysics, University of California, Santa Cruz, California 95064, USA

¹³Division of Geological and Planetary Sciences, California Institute of Technology, Pasadena, CA 91125, USA

¹⁴School of Earth & Space Exploration, Arizona State University, Tempe AZ 85287, USA

Accepted XXX. Received YYY; in original form ZZZ

ABSTRACT

The exoplanet WASP-12b is the prototype for the emerging class of ultra-hot, Jupiter-mass exoplanets. Past models have predicted—and near ultra-violet observations have shown—that this planet is losing mass. We present an analysis of two sets of 3.6 μ m and 4.5 μ m *Spitzer* phase curve observations of the system which show clear evidence of infrared radiation from gas stripped from the planet, and the gas appears to be flowing directly toward or away from the host star. This accretion signature is only seen at 4.5 μ m, not at 3.6 μ m, which is indicative either of CO emission at the longer wavelength or blackbody emission from cool, \lesssim 600 K gas. It is unclear why WASP-12b is the only ultra-hot Jupiter to exhibit this mass loss signature, but perhaps WASP-12b’s orbit is decaying as some have claimed, while the orbits of other exoplanets may be more stable; alternatively, the high energy irradiation from WASP-12A may be stronger than the other host stars. We also find evidence for phase offset variability at the level of 6.4σ (46.2°) at 3.6 μ m.

Key words: planets and satellites: individual (WASP-12b) – planet-star interactions – accretion, accretion discs – techniques: photometric

1 INTRODUCTION

The exoplanet WASP-12b (Hebb et al. 2009) is one of the hottest planets known to date and, as a result of its exceedingly tight orbit and inflated radius (a/R_* = 3.039, R_p = 1.900 R_J ; Collins et al. 2017), it is one of the best-

studied exoplanets. WASP-12b is also the archetype of an emerging class of exoplanets called ultra-hot Jupiters (UHJs). Planets in this regime are so strongly irradiated by their host star that many of the molecules (e.g., H₂ & H₂O) in their dayside atmospheres thermally dissociate (Bell et al. 2017; Bell & Cowan 2018; Arcangeli et al. 2018; Kreidberg et al. 2018; Lothringer et al. 2018; Mansfield et al. 2018; Parmentier et al. 2018) and may recombine nearer the nightside

★ E-mail: taylor.bell@mail.mcgill.ca (TJB)

(Bell & Cowan 2018; Komacek & Tan 2018; Parmentier et al. 2018). UHJs also bear some similarities to cataclysmic variable star (CV) systems and may undergo significant tidal distortion and mass loss, depending on the specifics of the star-planet system (e.g., Bisikalo et al. 2013a; Burton et al. 2014).

While tidal distortion is expected for WASP-12b, a 2010 *Spitzer* Infrared Array Camera (IRAC) thermal phase curve observation of WASP-12b at 4.5 μm demonstrated second order sinusoidal variations (with two maxima per planetary orbit) that were far greater than predicted (Cowan et al. 2012). The substellar axis would have to be 1.8 times as long as the dawn–dusk and polar axes if the observed variations were entirely due to the tidally distorted shape of the planet. Additionally, no evidence of these second order sinusoidal variations was found in a *Spitzer*/IRAC 3.6 μm phase curve also taken in 2010 (Cowan et al. 2012).

In this paper, we combine a new set of phase curves taken in 2013 with a reanalysis of the data from 2010 to determine the source of the unusually strong second order sinusoidal variations at 4.5 μm reported by Cowan et al. (2012). The observations are described in Section 2. Our three astrophysical models are described in Section 3.1, and our three independent reduction and decorrelation methods are described in Section 3.2. Results and their physical implications are presented in Section 4, and Section 5 contains the discussion and conclusion.

2 OBSERVATIONS

We combine two sets of two-channel (3.6 μm and 4.5 μm) *Spitzer*/IRAC observations taken in 2010 (PID 70060, PI Machalek) and 2013 (PID 90186, PI Todorov), all during the Post-Cryogenic *Spitzer* Mission. In all four phase curves, the system was observed nearly-continuously for \sim 33 hours (breaking only once or twice to repoint the telescope), beginning shortly before one secondary eclipse and ending shortly after the subsequent secondary eclipse. The reduced and detrended observations are shown in Figure 1.

For both data sets, the sub-array mode was used with 2 s exposures which produced data cubes of 64 images with 32×32 pixel ($39'' \times 39''$) dimensions. The 2010 observations were divided into 2 Astronomical Observation Requests (AORs) with a total of 902 data cubes (57 728 exposures), while the 2013 observations were divided into 3 AORs with a total of 909 data cubes (58 176 exposures). The 2010 full-phase observations were published by Cowan et al. (2012), the eclipse timings from the 2013 observations were published by Patra et al. (2017), and some derived parameters from all four phase curves were published as part of a broad comparison between different planets (Zhang et al. 2018).

Past observations of WASP-12 show a nearby M-dwarf binary system WASP-12B,C 1.''06 away from WASP-12A (Bergfors et al. 2011; Crossfield et al. 2012b; Bechter et al. 2014). As this binary system lies too close to WASP-12A to be resolved by *Spitzer*, we correct for blended light after analyzing the light curves, following past work (Stevenson et al. 2014a); see Appendix A for more details.

3 LIGHT CURVE ANALYSIS

3.1 Astrophysical Models

We model the observations as

$$F_{\text{model}}(t) = A(t) \times \tilde{D}(t)$$

where $\tilde{D}(t)$ is the normalized detector model; see Section 3.2 for details on the specific models used which consist of both parametric (2D polynomials and pixel level decorrelation) and non-parametric models (bilinear interpolated subpixel sensitivity mapping). The astrophysical model is

$$A(t) = F_*(t) + F_p(t),$$

where F_* is the flux from the host star (assumed to be constant except during transits) and F_p is the planetary flux. Transits and eclipses are modelled using `batman` (Kreidberg 2015), assuming a quadratic limb-darkening model for the host star and a uniform disk for the planet. The planetary flux is modelled as

$$F_p(t) = F_{\text{day}}\Phi(\psi(t)),$$

where F_{day} is the instantaneous eclipse depth at phase 0.5 (assumed to be constant over each \sim 33 hour phase curve), Φ describes the phase variations, and the orbital phase with respect to eclipse is $\psi(t) = 2\pi(t - t_e)/P$, where t_e is the time of eclipse and P is the planet’s orbital period.

We consider three different models for the astrophysical phase variations in the lightcurve. The simplest astrophysical model we consider is a first order sinusoid

$$\Phi_1(\psi) = 1 + C_1 \left(\cos(\psi) - 1 \right) + D_1 \sin(\psi),$$

and we also consider a second order sinusoid

$$\Phi_2(\psi) = \Phi_1(\psi) + C_2 \left(\cos(2\psi) - 1 \right) + D_2 \sin(2\psi),$$

where C_1 , D_1 , C_2 , and D_2 are all constants. If the previously reported double peaked phase curve (Cowan et al. 2012) is astrophysical in nature, one potential interpretation is that some/all of the power in the second order sinusoidal variations is from tidal distortion of the planet. We model this scenario with

$$\Phi_{1,\text{ellipsoid}}(\psi) = S(\psi)\Phi_1(\psi),$$

where $S(\psi)$ describes the projected area of an ellipsoid as it rotates. Rather than model a triaxial ellipsoid, we constrain the polar and dawn–dusk axes to share the same length since rotational deformation is expected to be negligible compared to tidal deformation (Leconte et al. 2011a). To find the deviations in the projected area of this biaxial ellipsoid, we adapt an equation from past work (Leconte et al. 2011b),

$$S(\psi) = \left[\sin^2(i) \left(\left(\frac{R_{p,2}}{R_p} \right)^2 \sin^2(\psi) + \cos^2(\psi) \right) + \left(\frac{R_{p,2}}{R_p} \right)^2 \cos^2(i) \right]^{1/2},$$

where i is the orbital inclination, R_p is the planetary radius along the polar and dawn–dusk axes (the two axes observed during transit and eclipse if $i = 90^\circ$), and $R_{p,2}$ is the planetary radius along the line connecting the planet and star (the sub-stellar axis).

3.2 Decorrelation Procedures

To ensure our results are robust and independent of the methods used, we perform three independent reductions and analyses following previously employed methods (Zhang et al. 2018; Dang et al. 2018; Cubillos et al. 2014) which are summarized below. Each analysis considers all three phase variation models. Within each analysis pipeline, models are selected based on the Bayesian Information Criterion (BIC). We cannot choose our fiducial models between our three analyses using the BIC as there are significant differences between the number of data used in each analysis because of different σ -clipping and binning. Instead, we choose to discriminate between the three analyses by selecting the model with the largest log-likelihood per datum, $\ln(L)/N_{\text{data}}$; we therefore adopt the preferred models from M. Zhang’s analyses as our fiducial models. The fiducial reductions of the four data sets are presented in Figure 1 and Table 1 (see also the Appendix and Supplementary Information).

3.2.1 Fiducial Reduction and Decorrelation Procedure

For reasons described below, M. Zhang’s analyses were selected as our fiducial analyses and follow their previous work (Zhang et al. 2018). In this analysis, we perform aperture photometry with a radius of 2.7 pixels on the *Spitzer* BCD files to get the raw flux for all frames. The background is calculated by excluding all pixels within a radius of 12 pixels from the star, rejecting outliers using sigma clipping, and then calculating the biweight location of the remaining pixels. We then bin the background-subtracted raw fluxes with a bin size of 64, discard the first 0.05 days of data, and perform fitting with `emcee` (Foreman-Mackey et al. 2013). The fitting uses 250 walkers that walk for 20 000 burn-in steps and 20 000 post-burn-in steps. Our instrumental model uses first order PLD for all data except the 2010 3.6 μm data, in which case we find that second order PLD minimizes BIC. Aside from PLD, the instrumental model also includes a linear slope with respect to time. We fit for the following parameters, all with uniform priors: transit time, eclipse time, R_p/R_* , eclipse depth (assumed to be constant over each ~ 33 hour phase curve), sinusoidal phase variation amplitudes (C_1 and D_1 for the first order sinusoid, and C_2 and D_2 if running a second order sinusoidal model), photometric error, slope in flux with time, and PLD coefficients. a/R_* and i are fixed to the highly precise values from the literature (Collins et al. 2017). As limb darkening is not that important in the *Spitzer* bands, we adopt the closest model from a grid of 1D stellar models (Sing 2010).

Our fiducial analyses find that the photon noise limits are 652 ppm and 637 ppm for the 2010 and 2013 3.6 μm observations, respectively, and the limits for the 2010 and 2013 4.5 μm observations are 866 ppm and 860 ppm, respectively. The differences between these two is likely due to the star falling on parts of the detector with slightly different sensitivities, as well as varying aperture sizes. The fitted photometric standard deviation from our fiducial analyses are 950 ppm and 976 ppm for the 2010 and 2013 3.6 μm observations (1.46 and 1.53 times greater than the photon noise limit). For the 2010 and 2013 4.5 μm observations, the fitted photometric standard deviations are 1134 ppm and 1158 ppm (1.31 and 1.35 times greater than the photon

noise limit). Figures showing the normalized raw, decorrelated, and residual fluxes from all four phase curves analyzed with M. Zhang’s pipeline can be found in the Appendix (Figures A6 and A7).

3.2.2 T. Bell’s Reduction and Decorrelation Procedure

Reduction and decorrelation of these data follow Dang et al. (2018) and are summarized here. We convert the pixel intensity from MJy/str to electron counts and mask bad pixels, i.e., 4σ outliers with respect to the median of that pixel in the datacube as well as any NaN pixels. We discard all frames with a bad pixel within the aperture used for photometry. We also discard every first frame from each data cube from the 2010 observations and every first and second frame from each data cube for the 2013 observations because these frames consistently show the presence of significant outliers compared to other frames within the same data cube. The effect of this sigma clipping is minimal, given that model fitting is performed on the median binned values from each data cube. There is another star (other than WASP-12A,B,C) that falls on the detector but lies outside the considered photometric apertures ($\sim 10''$ away); we place a 3×3 pixel mask around this star to ensure that it does not bias the background subtraction.

We then perform aperture photometry on each individual frame, with an aperture at the fixed pixel-location (15,15), and centroids were found using a flux-weighted mean algorithm and later used for decorrelation. Apertures ranging from 2 to 5 pixels in radius were considered as well as two different aperture edges: hard (the pixel’s flux is included if the centre of the pixel lies within the aperture) and soft (each pixel is weighed by the exact fraction of its area included within the aperture). While some flux will be lost by smaller apertures, a smaller aperture better allows us to remove intra-pixel sensitivity variations, which are the dominant source of noise in our data. We select the aperture radius and edge which resulted in the lowest RMS after a copy of the raw data were smoothed by a boxcar filter of width 5 data cubes (~ 11 minutes which is approximately half the ingress/egress duration) to remove features such as transits, eclipses, and phase variations. Tests run with apertures centred on the flux-weighted mean derived centroids showed that the RMS was > 100 ppm higher than the fixed position apertures. For the 2010 data, we selected a hard-edged 2.5 pixel radius aperture for the 4.5 μm data and a soft-edged 4.3 pixel radius aperture for the 3.6 μm data; the previous analysis of these data (Cowan et al. 2012) used IDL’s approximation on a soft-edged 2.5 pixel radius aperture for both wavelengths. For the 2013 data, we selected a hard-edged 3.2 pixel radius aperture for the 4.5 μm data and a soft-edged 2.9 pixel radius aperture for the 3.6 μm data. Before decorrelating and analyzing the data, we first bin the flux and centroid measurements from all 64 frames within a data cube using a median to reduce noise and decrease computation time. On average, each of our models take ~ 0.5 hour to fit to the binned data, and computation time grows linearly with the number of data points, so running each of the different models on unbinned data is not feasible.

T. Bell’s analyses used various systematic models as implemented in the open-source *Spitzer* Phase Curve Anal-

ysis (SPCA; Dang et al. 2018) pipeline¹. In particular, we used two-dimensional polynomials of order 2 through 5 and BiLinear Interpolated Subpixel Sensitivity (BLISS) mapping. The two-dimensional polynomials (Charbonneau et al. 2008) assume the sensitivity of the detector can be described by an n th-order 2D polynomial in the measured centroid. BLISS mapping (Stevenson et al. 2012a; Ingalls et al. 2016; Schwartz & Cowan 2017) is a non-parametric method to account for the intra-pixel sensitivity variations which requires accurate centroid measurements; when fitting BLISS models we adopt an 8×8 grid of knots. For the 2013 observations at 3.6 μm , we also needed to add a slope in time to remove residual red noise.

Models were fit using the Markov Chain Ensemble Sampler `emcee` (Foreman-Mackey et al. 2013). The orbital parameters of WASP-12b in the literature (Collins et al. 2017) have smaller errors than we can achieve with our photometry. Additionally, numerous searches for eccentricity have found that WASP-12b’s orbit is best described by a circular orbit (Campo et al. 2011; Croll et al. 2011; Bailey & Goodman 2018). Therefore, we set the orbital eccentricity to zero, fixed the orbital period to 1.09142030 days (Collins et al. 2017), and used the following Gaussian priors: $t_0 = 56176.16825800 \pm 0.00007765$ (BMJD), $a/R_* = 3.039 \pm 0.034$, $i = 83.37^\circ \pm 0.68^\circ$ (Collins et al. 2017). The parameters that were always fitted were t_0 , R_p/R_* , a/R_* , i , F_{day}/F_* , two quadratic limb darkening parameters (Kipping 2013) q_1 and q_2 , and the first order sinusoidal amplitudes C_1 and D_1 . In some models, we also fitted $R_{p,2}/R_*$ or C_2 and D_2 . A number of detector parameters were also fitted, with the exact number depending on the detector model used.

For T. Bell’s apertures, the photon noise limits are 578 ppm and 566 ppm for the 2010 and 2013 3.6 μm observations, respectively, and the limits for the 2010 and 2013 4.5 μm observations are 795 ppm and 791 ppm, respectively. The fitted photometric standard deviation from T. Bell’s analysis are 1493 ppm and 1246 ppm for the 2010 and 2013 3.6 μm observations (2.58 and 2.20 times greater than the photon noise limit). For the 2010 and 2013 4.5 μm observations, the fitted photometric standard deviations are both 1440 ppm (1.81 and 1.82 times greater than the photon noise limit). The fitted data and red noise tests from these analyses can be found in the Supplementary Information (Figures A8 and A9).

3.2.3 P. Cubillos’ Reduction and Decorrelation Procedure

The models run by P. Cubillos use the Photometry for Orbits, Eclipses, and Transits (POET) pipeline (Stevenson et al. 2010; Stevenson et al. 2012a,b; Campo et al. 2011; Nymeyer et al. 2011; Cubillos et al. 2013, 2014). The POET pipeline starts by flagging bad pixels from the Spitzer BCD files using the permanent bad pixel masks and performing a sigma-rejection routine. Next, it estimates the target center position either fitting a two-dimensional Gaussian function or calculating the least asymmetry (Lust et al. 2014). Then it obtains raw light curves by applying a circular interpolated

aperture photometry, testing several aperture radii between 2.0 and 4.0 pixels.

To determine the optimal centroiding method and photometry aperture, POET minimizes the standard deviation of the residuals, and minimizes time-correlated noise at timescales equal and larger than the transit duration (estimated through the time-averaging method). Least asymmetry centroiding outperformed Gaussian centring for all datasets, except the 2013 4.5 μm observation. The optimal apertures were 2.5 and 3.0 pixels (2010) and 4.0 and 2.0 pixels (2013) for the 3.6 and 4.5 μm observations, respectively. In any case, all relevant astrophysical parameters vary within their uncertainties as we vary the centroiding and photometry.

POET models the unbinned light curves, simultaneously fitting the astrophysical phase curve and the telescope systematics. The systematics model consists of the non-parametric BLISS intrapixel model, for which we set the map’s bin size equal to the RMS of the frame-to-frame target position (0.01 pixels), and require at least 8 points per bin. For the 2013 4.5 μm observation, we also apply a linear time-dependent ramp with the slope as a free parameter.

The astrophysical model consists of transit and eclipse models (Mandel & Agol 2002), combined with the sinusoidal and ellipsoid models described in the Methods section. The transit free fitting parameters are the epoch, ratio between the planetary and stellar radii, cosine of inclination, semi-major axis to stellar radius ratio, stellar flux, and quadratic limb-darkening coefficients. The eclipse free fitting parameters are the midpoint, duration, depth, and ingress duration (setting the egress duration equal to the ingress duration). We adopt uniform priors for all parameters, except for $\cos(i)$ and a/R_* , which have Gaussian priors, and kept the orbital period fixed (same values as in T. Bell’s reduction and decorrelation procedure; Collins et al. 2017).

POET incorporates the MC3 statistical package (Cubillos et al. 2017) to find the best-fitting parameter values (using Levenberg-Marquardt optimization) and uncertainties (using a differential-evolution Markov Chain Monte Carlo algorithm; ter Braak & Vrugt 2008), requiring the Gelman-Rubin statistic (Gelman & Rubin 1992) to be within 1% of unity for each free parameter for convergence. POET uses Bayesian hypothesis testing to select the model best supported by the data, selecting the lowest BIC model. The POET results support the independent results of the other pipelines. Both 4.5 μm observations strongly favour the second order sinusoidal model, while both 3.6 μm observations strongly favour the first order sinusoidal model.

For P. Cubillos’ apertures, the photon noise limits are 4886 ppm and 6664 ppm for the 2010 and 2013 3.6 μm observations, respectively, and the limits for the 2010 and 2013 4.5 μm observations are 8273 ppm and 7988 ppm, respectively. The fitted photometric standard deviation from P. Cubillos’ analysis are 6915 ppm and 7360 ppm for the 2010 and 2013 3.6 μm observations (1.41 and 1.10 times greater than the photon noise limit). For the 2010 and 2013 4.5 μm observations, the fitted photometric standard deviations are 9130 ppm and 8658 ppm (1.10 and 1.08 times greater than the photon noise limit). The fitted data and red noise tests from these analyses can be found in the Supplementary Information (Figures A10 and A11).

¹ <https://github.com/lisadang27/SPCA>

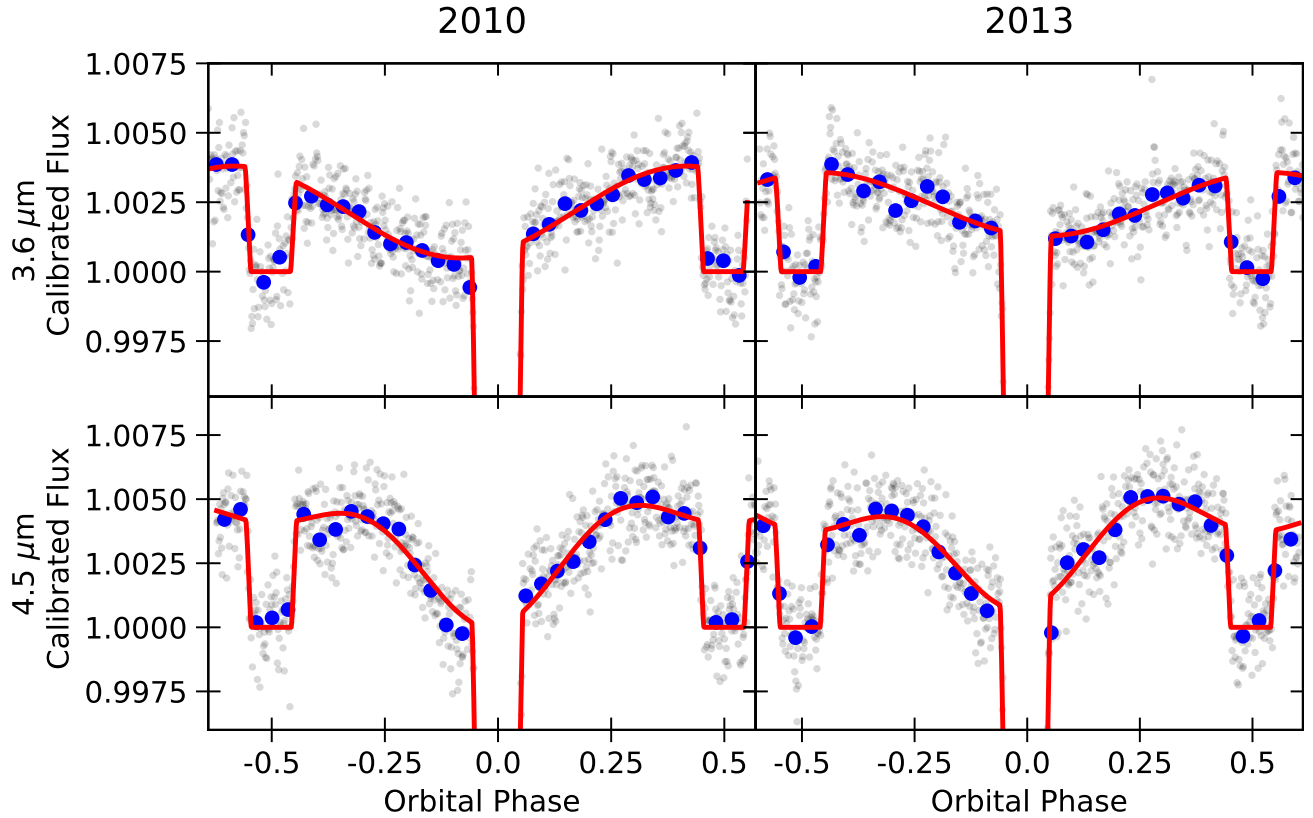


Figure 1. Fiducial analyses of $3.6\text{ }\mu\text{m}$ (top) and $4.5\text{ }\mu\text{m}$ (bottom) *Spitzer*/IRAC phase curve observations of WASP-12b taken in 2010 (left) and 2013 (right). Both $3.6\text{ }\mu\text{m}$ phase curves show one maximum per planetary orbit, while both $4.5\text{ }\mu\text{m}$ phase curves exhibit two maxima per planetary orbit. The detector systematics have been removed from the data, and our fiducial astrophysical models for each data set are overplotted in red. Grey data points show binned values from each *Spitzer* data cube (64 frames), and the blue points show more coarsely binned values (1664 frames).

Table 1. Key fiducial light curve parameters

Data Set	R_p/R_* [‡]	1st Order	2nd Order	F_{day}/F_* [‡] (ppm)
		Phase Offset [†] (degrees)	Phase Offset [†] (degrees)	
2010, $3.6\text{ }\mu\text{m}$	0.11642 ± 0.00063	-32.6 ± 6.2	—	3870 ± 130
2013, $3.6\text{ }\mu\text{m}$	0.11327 ± 0.00068	13.6 ± 3.8	—	3840 ± 120
2010, $4.5\text{ }\mu\text{m}$	0.10656 ± 0.00085	-9.5 ± 2.3	94.7 ± 1.6	4360 ± 140
2013, $4.5\text{ }\mu\text{m}$	0.1049 ± 0.0010	-19.1 ± 3.9	93.2 ± 1.9	3920 ± 150

[†] These phase offsets are measured in degrees *after* eclipse and are derived quantities.

[‡] These quantities have been corrected for dilution from WASP-12BC (see Appendix A).

4 RESULTS

4.1 Comparison Between Pipelines and Epochs

All three independent analyses confirm the presence of strong and persistent second order sinusoidal variations at $4.5\text{ }\mu\text{m}$ and the non-detection of these variations at $3.6\text{ }\mu\text{m}$. The fitted phase curves parameters for the preferred models from all three independent pipelines are summarized in Figure 1 and Table A1. See the Supplementary Information for tabulated values for all considered models. The astrophysical parameters at $3.6\text{ }\mu\text{m}$ and $4.5\text{ }\mu\text{m}$ are mostly consistent

between all three analyses, with the preferred models from the three analyses generally differing by $< 2\sigma$. In the few cases where one model differs from the others by more than 2σ , the other two models are consistent with each other at a level of $< 1\sigma$. Also, there is low-frequency noise in the 2010 $4.5\text{ }\mu\text{m}$ residuals between the first eclipse and the end of the transit that is seen by all three analysis pipelines; the source of these variations is not understood.

From 2010 to 2013, the three pipelines show that all $4.5\text{ }\mu\text{m}$ phase curve and planetary parameters remain constant within $< 2\sigma$. Most of the phase curve and planetary

parameters at $3.6\text{ }\mu\text{m}$ also remain constant between the two observing epochs, with the main exception being the phase offset calculated using the first order sinusoidal terms. M. Zhang's, P. Cubillos', and T. Bell's pipelines find that it changes by 6.4σ (46.2°), 7.7σ (46.6°), and 3.1σ (28.1°), respectively. All three pipelines also agree that the sign of the hotspot offset changes between the two observing epochs, with the offset being "eastward" (before eclipse) in 2010 and "westward" (after eclipse) in 2013. It is interesting to note, however, that over this same time span both the first and second order sinusoidal phase offsets from the $4.5\text{ }\mu\text{m}$ observations do not change. No other parameter is found by all three analyses to vary by more than 3σ between the two observing epochs. Finally, if the first order sinusoidal phase variations are entirely attributable to WASP-12b's temperature map, our 2013 observations at $3.6\text{ }\mu\text{m}$ exhibit a $13.6^\circ \pm 3.8^\circ$ westward hotspot offset. This may be a demonstration that eastward hotspot offsets are less ubiquitous than previously believed, with westward hotspot offsets reported for planets with irradiation temperatures spanning 2200 – 3700 K (Dang et al. 2018; Zhang et al. 2018; Wong et al. 2016).

4.2 Physical Sources

The previously favoured explanation for the double peaked phase curve reported for WASP-12b by Cowan et al. (2012) was detector systematics, but this hypothesis is now strongly disfavoured. To date, 23 papers have been published with new *Spitzer* phase curves of 18 different exoplanets (Harrington et al. 2006; Knutson et al. 2007; Cowan et al. 2007; Knutson et al. 2009b,a; Laughlin et al. 2009; Crossfield et al. 2010; Cowan et al. 2012; Knutson et al. 2012; Crossfield et al. 2012a; Lewis et al. 2013; Maxted et al. 2013; Zellem et al. 2014; Wong et al. 2015; de Wit et al. 2016; Wong et al. 2016; Krick et al. 2016; Demory et al. 2016; Wong et al. 2016; Stevenson et al. 2017; de Wit et al. 2017; Zhang et al. 2018; Dang et al. 2018; Kreidberg et al. 2018). Of these numerous observations, WASP-12 is the only system which has shown strong a double peaked phase curve not once, but twice. The observing strategy also differed between these two sets of WASP-12b phase curves, with the number and timing of AORs changing and the addition of PCRS Peak-Up before the 2013 observations. The consistency between the two sets of phase curves suggests that the observations probe an astrophysical source which does not vary significantly over a ~ 3 year timescale. Cowan et al. (2012) suggested that tidal distortion and/or mass loss might be able to explain the *Spitzer* observations, if this signal was indeed astrophysical in nature. We explore these and other potential sources of emission below.

4.2.1 Tidal Distortion

One potential cause of second order sinusoidal variations is tidal deformation of the host star, as is seen at optical wavelengths for HAT-P-7 (Welsh et al. 2010) and WASP-18 (Shporer et al. 2019). However, stellar distortion is expected to be negligible for WASP-12 (Leconte et al. 2011a). We verified this by numerically solving for the equipotential stellar/planetary surfaces using the dimensionless Roche potential (see Appendix C). However, since the star contributes

significantly more flux than the planet, we ran simple simulations of both the star and planet including the effects of gravity darkening to assess their expected amplitudes of ellipsoidal variations. We find that the stellar ellipsoidal variations are approximately the same amplitude at $3.6\text{ }\mu\text{m}$ and $4.5\text{ }\mu\text{m}$ and the amplitude of the stellar variations are far smaller than the observed amplitudes; we therefore conclude that tidal bulges on the host star cannot be the source of the strong second order variations observed at $4.5\text{ }\mu\text{m}$. Our predicted ellipsoidal variations for WASP-12b are consistent with our limits on second order sinusoidal variations at $3.6\text{ }\mu\text{m}$, but significantly under-predict the observed amplitude at $4.5\text{ }\mu\text{m}$ (also see the implied dimensions of the best-fit ellipsoidal variation model shown in the right panel of Figure 2). If we interpret the second order sinusoidal variations at $4.5\text{ }\mu\text{m}$ as planetary ellipsoidal variations, this would require the $4.5\text{ }\mu\text{m}$ photosphere to be significantly higher up than $3.6\text{ }\mu\text{m}$ as the layers nearer the Roche lobe are more distorted. However, this increased radius at $4.5\text{ }\mu\text{m}$ is inconsistent with the smaller transit depth at $4.5\text{ }\mu\text{m}$ compared to $3.6\text{ }\mu\text{m}$. We therefore conclude that tidal distortion of the planet is also not the source of the strong second order variations observed at $4.5\text{ }\mu\text{m}$.

4.2.2 Stellar Variability and Inhomogeneities

Stellar variability is also unlikely to be the cause of these observations given the comparable phase of the second order variations in the two data sets. For reference, the WASP-12BC dilution correction term is ~ 400 ppm while the observed amplitude of the second order sinusoidal variations is ~ 2000 ppm. Additionally, variability in WASP-12A is only predicted to modulate the planetary signal at a level of ~ 1 ppm, and variability in WASP-12B,C should also only contribute at the level of ~ 1 ppm (while these M-dwarfs should be $\sim 10\times$ more variable, they contribute $\sim 10\times$ less flux; Zellem et al. 2017). We therefore rule out standard stellar variability as the source of the strong second order sinusoidal variations seen at $4.5\text{ }\mu\text{m}$. If the second order variations were produced by unusually strong inhomogeneities on the host star, both the sub-planet longitude and the anti-planet longitude would need to be darker than intermediate longitudes — this would imply star–planet interactions. However, these inhomogeneities would also need to be much more pronounced at $4.5\text{ }\mu\text{m}$ which would not be expected for the $\sim 6000\text{ K}$ star.

4.2.3 Mass Loss

There is significant observational evidence from near ultraviolet (NUV) transit observations that WASP-12b is undergoing mass loss and that there is a bow shock in the system (Fossati et al. 2010; Haswell et al. 2012; Nichols et al. 2015) (see the Supplementary Information). A potential explanation for the unusual $4.5\text{ }\mu\text{m}$ phase curve is that there is gas being stripped from the planet which emits more strongly within the $4.5\text{ }\mu\text{m}$ bandpass than the $3.6\text{ }\mu\text{m}$ bandpass. The observations favour a stream of dense gas stripped from the planet flowing directly toward/away from the host star or some other elongated patch of hot gas whose long axis is parallel to the star–planet axis, such as an accretion hot

spot. Double-peaked phase curves have been seen for dwarf novae CVs, such as WZ Sge (Skidmore et al. 1997), however this feature was seen through the ultra-violet to infrared; for CVs these variations have been attributed to tidal distortion or an optically thick hot spot in an otherwise optically thin accretion disk (e.g., Skidmore et al. 1997)

The source of the 4.5 μm variations in the WASP-12 system must lie near the star–planet axis since there is no significant detection of an occultation of the source when the planet is not in transit or eclipse. Additionally, our *Spitzer* observations demonstrate that the planetary radius appears $\sim 8\%$ (11σ) smaller at 4.5 μm than at 3.6 μm which is in disagreement with model predictions (Burrows et al. 2007, 2008; Cowan et al. 2012); this rules out the transit of a large exosphere that is opaque at 4.5 μm as this would make the planetary radii at the two wavelengths even more discrepant.

As shown in Table 1, the fitted second order offsets at 4.5 μm are consistent with being oriented along the star–planet axis (90°). However, previously published 3D magnetohydrodynamic (MHD) numerical simulations of hypothetical exoplanet systems mostly produced gas flows that significantly lead the star–planet axis (Matsakos et al. 2015). Indeed, gas streaming from the planet’s L1 Lagrange point on a ballistic trajectory should flow $\theta_{\text{gas}} = 53.4^\circ$ *ahead* of the star–planet axis (Lai et al. 2010) as angular momentum is conserved (see Figure 2 for a schematic depiction). Assuming our observations probe the gas stream, this prediction is 27σ discrepant with our offset of $4.0^\circ \pm 2.1^\circ$ *behind* the star–planet axis found by averaging the offsets from the two fitted second order sinusoids at 4.5 μm . This discrepancy could potentially be explained if the 4.5 μm emitting area is much closer to the planet and is still aligned along the star–planet axis and then becomes more diffuse and flows ahead of the planet as it continues to fall toward the host star.

Alternatively, stellar effects could channel the infalling stream directly toward the star, but this may be inconsistent with past NUV transit observations (Fossati et al. 2010; Haswell et al. 2012; Nichols et al. 2015). One previously published 3D MHD model (Matsakos et al. 2015) did exhibit a stream of gas directly along the star–planet axis (their name for this model was ‘FvrB’). This model has high stellar ultraviolet (UV) flux, a low escape speed from the planet, the planet near to its host star, and a strong planetary magnetic field. In this model, the planet is experiencing Roche lobe overflow with a planetary wind that is weak compared to the stellar wind, producing an approximately linear stream of gas along the star–planet axis as well as a lower density tail trailing behind the planet (Matsakos et al. 2015). The non-detection of the gas trailing behind the planet could be explained if the gas has a lower density and/or has a lower temperature. As the dense gas stream in the ‘FvrB’ model is aligned along the star–planet axis, it may not contribute significantly to the transit depth and may remain consistent with the smaller apparent radius at 4.5 μm compared to 3.6 μm . Radiative transfer simulations based on the ‘FvrB’ mass-loss model (Matsakos et al. 2015) would allow for this hypothesis to be tested.

4.3 Radiation Mechanisms

4.3.1 Blackbody Emission

The discrepant second order sinusoidal amplitudes at 3.6 μm and 4.5 μm can be explained by one of two emission mechanisms. First, blackbody emission could allow for greater flux at 4.5 μm than at 3.6 μm if the gas is sufficiently cool that the 3.6 μm bandpass lies on the Wien side of the blackbody curve; this scenario would allow us to place an upper limit on the temperature and spatial extent of the emitting gas, which we pursue below.

Using the host star’s effective temperature of 6300 ± 150 K (Hebb et al. 2009), we assume the host star emits as a blackbody and convert the second order sinusoidal curves from units of F_{day}/F_* to B_λ as shown in the middle panel of Figure 3. We adopt the fiducial 4.5 μm parameters from 2010, but set the phase offset to 90° since there is no evidence for an appreciable offset from the star–planet axis. We then take the best-fit and the 1σ and 2σ upper limits on the amplitude of the 3.6 μm second order sinusoidal variations from M. Zhang’s analysis using the second order astrophysical model. We assume that none of the flux seen during planetary transit/eclipse is from emission by the gas. By assuming the emitting area is the same at 3.6 μm and 4.5 μm , we can use the relative amounts of flux at these two wavelengths to determine the blackbody temperature of the gas.

Given the assumption that our observations are explained by blackbody emission, we can then place a 2σ upper limit of 619 K on the gas temperature. For reference, a temperature of 816 K would provide equal flux in both bandpasses. Attributing any of the ‘nightside’ flux to emission from the gas only lowers this limit further. Also, as WASP-12b’s skin temperature (Goody & Walker 1972) is $0.5^{0.25} T_{\text{b,day}} \approx 2500$ K, this gas cannot be the upper layers of the planet’s atmosphere.

By taking the ratio between the flux emitted by the gas and that emitted by the star, we can determine the effective emitting area required to produce the phase curve observations. As shown in the bottom panel of Figure 3, less emission at 3.6 μm requires lower temperature gas and therefore a larger emitting area. We can therefore place a 2σ lower-limit on the effective emitting area of the gas of 0.98 times the planet’s transiting area when seen at planetary quadrature, given the assumption that our observations are explained by blackbody emission. Attributing any of the nightside flux to emission from the gas slightly increases this limit and allows for a non-zero emitting area during planetary transit and eclipse.

4.3.2 CO Emission

An alternative explanation for the increased flux at 4.5 μm is emission by CO which has its strong $\Delta V = 1$ band around 4.5 μm (see Figure A2 in the Appendix for the CO line intensities); CO emission has previously been predicted for gas lost from WASP-12b (Li et al. 2010; Deming et al. 2011). The CO molecule should be dissociated in the planetary upper atmosphere due to the strong UV and X-ray flux from the host star which also drives most of the observed atmospheric escape seen at NUV wavelengths (Fossati et al.

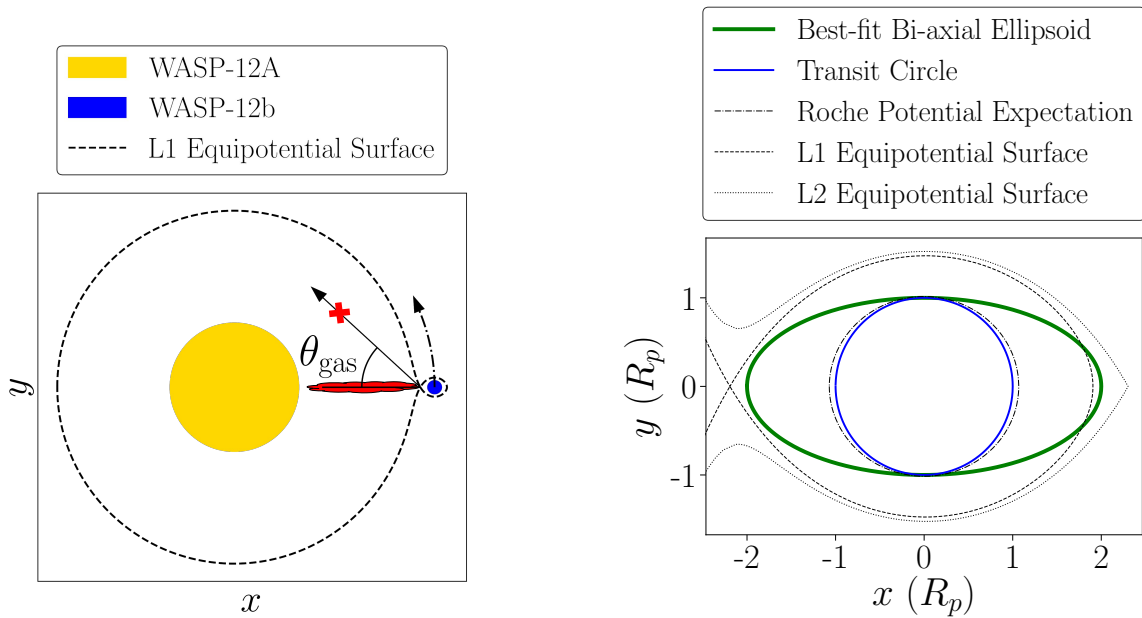


Figure 2. Bird's-eye views of the WASP-12 system to scale. *Left:* While the planet is appreciably filling its Roche lobe and is expected to be tidally distorted, the star should not. Over-plotted is a depiction of the direction that gas would flow after passing through the L1 Lagrange point (θ_{gas}) previously predicted to be 53.4° (Lai et al. 2010). If our observations probe the gas stream, we can firmly reject this ballistic trajectory hypothesis as the gas appears to be aligned along the star–planet axis (indicated by the red elongated patch of gas). The direction of the planet's orbit is shown with a dash-dotted arrow. *Right:* Best-fit bi-axial ellipsoid model fit to the 2013 phase curve observation at $4.5\ \mu\text{m}$, placed in the context of the planet's Roche lobe. This shape varies drastically from that of a Roche lobe and instead suggests that our observations are probing something other than the planet's tidally distorted shape. Also shown is a circle with the area seen at transit, the equipotential surface which would give that transit area, and the L1 and L2 equipotential surfaces. The x and y axes lie within the orbital plane; during transit the x -axis is parallel to our line of sight.

2010; Haswell et al. 2012; Nichols et al. 2015); the dissociation energy of CO corresponds to a wavelength of roughly $110\ \text{nm}$. However, the atomic carbon and oxygen from the upper layers of the planet's atmosphere could recombine in a gas stream where the density gets higher because of stellar wind confinement and the “shadow effect” from the material in the stream closer to the star. Given a gas temperature profile (Salz et al. 2016) and our calculations of the thermal dissociation fraction of CO using the Saha equation (Bell & Cowan 2018), we find that any CO emission must either be produced within $\sim 0.1\ R_p$ of the planet's surface or beyond $2.5\ R_p$. In the case of a bow shock supported by mass loss from the planet, gas temperatures are predicted to reach 10^3 – $10^4\ \text{K}$ (Turner et al. 2016) which should allow for stable CO, provided there is sufficient UV shielding from gas nearer to the star. Simulations of the behaviour of CO in these environments are required to determine the feasibility of this molecule recombining once in a stream and emitting sufficiently strongly to explain our observations.

5 DISCUSSION AND CONCLUSIONS

By independently analyzing and then combining two sets of $3.6\ \mu\text{m}$ and $4.5\ \mu\text{m}$ *Spitzer* phase curves of the UHJ WASP-12b, we have conclusively detected strong and persistent second order sinusoidal variations at $4.5\ \mu\text{m}$ and placed stringent upper limits on these variations at $3.6\ \mu\text{m}$. These observations of WASP-12b raise several questions which will require further study to resolve.

Our two emission hypotheses could be distinguished with phase curve observations of the $\sim 1.6\ \mu\text{m}$ and/or $2.29\ \mu\text{m}$ CO emission bands and/or with phase curve observations at wavelengths longer than $5\ \mu\text{m}$ which should exhibit strong second order sinusoidal variations if the $3.6\ \mu\text{m}$ vs. $4.5\ \mu\text{m}$ amplitude discrepancy is the result of black-body emission. The high precision and wavelength coverage achievable with the James Webb Space Telescope should allow these two emission hypotheses to be tested. The $\sim 1.6\ \mu\text{m}$ CO emission band also lies within the Hubble/WFC3 bandpass and may be detectable with phase curve observations.

Critically, future models must also address the fact that the fitted planetary radius is significantly smaller at $4.5\ \mu\text{m}$ than at $3.6\ \mu\text{m}$; this may be the result of unocculted emitting gas. Combined hydrodynamic and radiative transfer simulations are required to fully understand this system. These simulations will allow us to determine the location and spatial extent of the emitting gas, and they may resolve the apparent tension between the constraint from these observations that the gas is well aligned with the star–planet axis, while NUV observations which probe lower density gas show that the gas flows significantly ahead of the planet. Understanding the nature of the increased emission at $4.5\ \mu\text{m}$ will also require modelling the mass loss and the UV dissociation and potential recombination of CO molecules as they flow from the planet's upper atmosphere through a gas stream and potentially experience a shock. These models may also assist in understanding the observed hot spot variability seen at $3.6\ \mu\text{m}$.

Finally, while WASP-12b is one of the exoplanets clos-

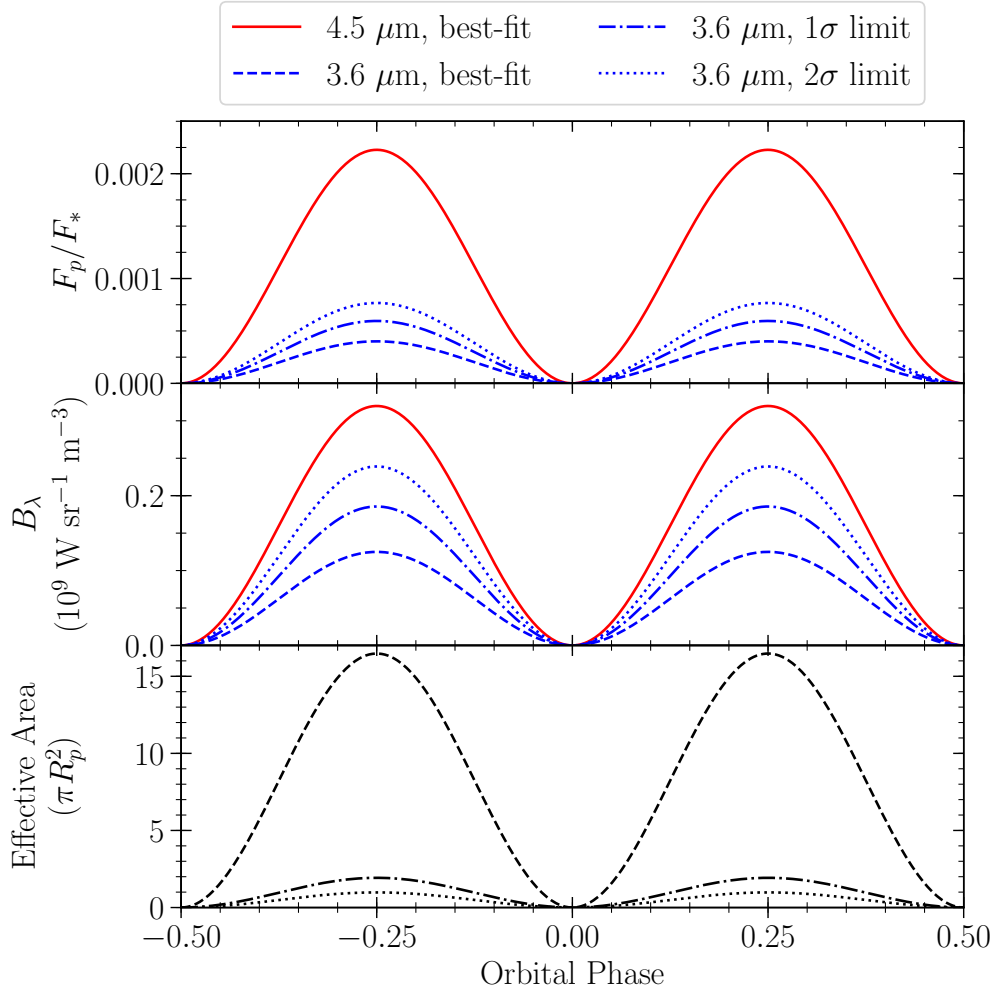


Figure 3. Limits on the emitting area required to explain the strong detection of second order sinusoidal variations at 4.5 μm but not at 3.6 μm . *Top*: the emitting-body to star flux ratio for the second-order sinusoidal component of the 4.5 μm and 3.6 μm data (temporarily assuming a constant radius of R_p). *Middle*: the emitting-body's blackbody flux assuming both wavelengths probe the same area. *Bottom*: the effective emitting area of the emitting blackbody required to explain the observations. The inferred gas temperatures for the 0σ , 1σ , and 2σ limits are 420 K, 549 K, and 619 K, respectively.

est to overflowing it's Roche lobe (see Figure A3), there are several others with similar characteristics with published Spitzer phase curves that do not show strong second order sinusoidal variations at 4.5 μm : particularly WASP-19b (Wong et al. 2016), WASP-33b (Zhang et al. 2018), and WASP-103b (Kreidberg et al. 2018). One potential explanation is that WASP-12b's orbit may be decaying (Maciejewski et al. 2016; Patra et al. 2017) while the other exoplanets may be more stable; alternatively, the high energy irradiation from WASP-12A may be stronger than the other host stars. Further research is required to understand why WASP-12b is the only exoplanet known to be exhibiting these exceptionally strong second order sinusoidal variations at 4.5 μm .

ACKNOWLEDGEMENTS

T.J.B. acknowledges support from the McGill Space Institute Graduate Fellowship, the Natural Sciences and Engineering Research Council of Canada's Postgraduate

Scholarships-Doctoral Fellowship, and from the Fonds de recherche du Québec – Nature et technologies through the Centre de recherche en astrophysique du Québec. We have also made use of open-source software provided by the Python, Astropy, SciPy, and Matplotlib communities.

REFERENCES

- Arcangeli J., et al., 2018, *ApJL*, 855, L30
- Armstrong D. J., de Mooij E., Barstow J., Osborn H. P., Blake J., Sanee N. F., 2016, *Nature Astronomy*, 1, 0004
- Artigau É., Bouchard S., Doyon R., Lafrenière D., 2009, *ApJ*, 701, 1534
- Bailey A., Goodman J., 2018, preprint, ([arXiv:1808.00052](https://arxiv.org/abs/1808.00052))
- Bechter E. B., et al., 2014, *ApJ*, 788, 2
- Bell T. J., Cowan N. B., 2018, *ApJL*, 857, L20
- Bell T. J., et al., 2017, *ApJL*, 847, L2
- Bergfors C., Brandner W., Henning T., Daemgen S., 2011, in Sozzetti A., Lattanzi M. G., Boss A. P., eds, IAU Symposium Vol. 276, The Astrophysics of Planetary Systems: For-

mation, Structure, and Dynamical Evolution. pp 397–398, doi:10.1017/S1743921311020503

Bisikalo D. V., Kaigorodov P. V., Ionov D. E., Shematovich V. I., 2013a, *Astronomy Reports*, **57**, 715

Bisikalo D., Kaigorodov P., Ionov D., Shematovich V., Lammer H., Fossati L., 2013b, *ApJ*, **764**, 19

Budaj J., 2011, *AJ*, **141**, 59

Burrows A., Hubeny I., Budaj J., Knutson H. A., Charbonneau D., 2007, *ApJL*, **668**, L171

Burrows A., Budaj J., Hubeny I., 2008, *ApJ*, **678**, 1436

Burton J. R., Watson C. A., Fitzsimmons A., Pollacco D., Moulds V., Littlefair S. P., Wheatley P. J., 2014, *ApJ*, **789**, 113

Campo C. J., et al., 2011, *ApJ*, **727**, 125

Charbonneau D., Knutson H. A., Barman T., Allen L. E., Mayor M., Megeath S. T., Queloz D., Udry S., 2008, *ApJ*, **686**, 1341

Cherenkov A. A., Bisikalo D. V., Kaigorodov P. V., 2014, *Astronomy Reports*, **58**, 679

Collins K. A., Kielkopf J. F., Stassun K. G., 2017, *AJ*, **153**, 78

Cowan N. B., Agol E., 2011, *ApJ*, **729**, 54

Cowan N. B., Agol E., Charbonneau D., 2007, *MNRAS*, **379**, 641

Cowan N. B., Machalek P., Croll B., Shekhtman L. M., Burrows A., Deming D., Greene T., Hora J. L., 2012, *ApJ*, **747**, 82

Cowan N. B., Fuentes P. A., Haggard H. M., 2013, *MNRAS*, **434**, 2465

Croll B., Lafreniere D., Albert L., Jayawardhana R., Fortney J. J., Murray N., 2011, *AJ*, **141**, 30

Crossfield I. J. M., Hansen B. M. S., Harrington J., Cho J. Y.-K., Deming D., Menou K., Seager S., 2010, *ApJ*, **723**, 1436

Crossfield I. J. M., Knutson H., Fortney J., Showman A. P., Cowan N. B., Deming D., 2012a, *ApJ*, **752**, 81

Crossfield I. J. M., Barman T., Hansen B. M. S., Tanaka I., Kodama T., 2012b, *ApJ*, **760**, 140

Cubillos P., et al., 2013, *ApJ*, **768**, 42

Cubillos P., Harrington J., Madhusudhan N., Foster A. S. D., Lust N. B., Hardy R. A., Bowman M. O., 2014, *ApJ*, **797**, 42

Cubillos P., Harrington J., Loredo T. J., Lust N. B., Blecic J., Stemm M., 2017, *AJ*, **153**, 3

Dang L., et al., 2018, *Nature Astronomy*, **2**, 220

Debrecht A., Carroll-Nellenback J., Frank A., Fossati L., Blackman E. G., Dobbs-Dixon I., 2018, *MNRAS*, **478**, 2592

Deming D., et al., 2011, *ApJ*, **726**, 95

Demory B.-O., Gillon M., Madhusudhan N., Queloz D., 2016, *MNRAS*, **455**, 2018

Espinosa Lara F., Rieutord M., 2011, *A&A*, **533**, A43

Foreman-Mackey D., et al., 2013, emcee: The MCMC Hammer, Astrophysics Source Code Library (ascl:1303.002)

Fossati L., et al., 2010, *ApJL*, **714**, L222

Fossati L., Ayres T. R., Haswell C. A., Bohlender D., Kochukhov O., Flöer L., 2013, *ApJL*, **766**, L20

Gelman A., Rubin D. B., 1992, *Statistical Science*, **7**, 457

Goody R., Walker J., 1972, *Atmospheres, Foundations of Earth Science Series*. Prentice-Hall, Englewood Cliffs, New Jersey

Harrington J., Hansen B. M., Luszcz S. H., Seager S., Deming D., Menou K., Cho J. Y.-K., Richardson L. J., 2006, *Science*, **314**, 623

Haswell C. A., et al., 2012, *ApJ*, **760**, 79

Hebb L., et al., 2009, *ApJ*, **693**, 1920

Husser T.-O., Wende-von Berg S., Dreizler S., Homeier D., Reiners A., Barman T., Hauschildt P. H., 2013, *A&A*, **553**, A6

Ingalls J. G., et al., 2016, *AJ*, **152**, 44

Kipping D. M., 2013, *MNRAS*, **435**, 2152

Knutson H. A., et al., 2007, *Nature*, **447**, 183

Knutson H. A., et al., 2009a, *ApJ*, **690**, 822

Knutson H. A., Charbonneau D., Cowan N. B., Fortney J. J., Showman A. P., Agol E., Henry G. W., 2009b, *ApJ*, **703**, 769

Knutson H. A., Howard A. W., Isaacson H., 2010, *ApJ*, **720**, 1569

Knutson H. A., et al., 2012, *ApJ*, **754**, 22

Komacek T. D., Tan X., 2018, *Research Notes of the American Astronomical Society*, **2**, 36

Kreidberg L., 2015, *PASP*, **127**, 1161

Kreidberg L., et al., 2018, *AJ*, **156**, 17

Krick J. E., et al., 2016, *ApJ*, **824**, 27

Lai D., Helling C., van den Heuvel E. P. J., 2010, *ApJ*, **721**, 923

Laughlin G., Deming D., Langton J., Kasen D., Vogt S., Butler P., Rivera E., Meschiari S., 2009, *Nature*, **457**, 562

Leconte J., Lai D., Chabrier G., 2011a, *A&A*, **528**, A41

Leconte J., Lai D., Chabrier G., 2011b, *A&A*, **536**, C1

Lewis N. K., et al., 2013, *ApJ*, **766**, 95

Li S.-L., Miller N., Lin D. N. C., Fortney J. J., 2010, *Nature*, **463**, 1054

Llama J., Wood K., Jardine M., Vidotto A. A., Helling C., Fossati L., Haswell C. A., 2011, *MNRAS*, **416**, L41

Lothringer J. D., Barman T., Koskinen T., 2018, *ApJ*, **866**, 27

Lust N. B., Britt D., Harrington J., Nymeyer S., Stevenson K. B., Ross E. L., Bowman W., Fraine J., 2014, *PASP*, **126**, 1092

Maciejewski G., et al., 2016, *A&A*, **588**, L6

Madhusudhan N., et al., 2011, *Nature*, **469**, 64

Mandel K., Agol E., 2002, *ApJL*, **580**, L171

Mansfield M., et al., 2018, *AJ*, **156**, 10

Matsakos T., Uribe A., Königl A., 2015, *A&A*, **578**, A6

Maxted P. F. L., et al., 2013, *MNRAS*, **428**, 2645

Nichols J. D., et al., 2015, *ApJ*, **803**, 9

Nymeyer S., et al., 2011, *ApJ*, **742**, 35

Parmentier V., et al., 2018, *A&A*, **617**, A110

Patra K. C., Winn J. N., Holman M. J., Yu L., Deming D., Dai F., 2017, *AJ*, **154**, 4

Radigan J., Jayawardhana R., Lafrenière D., Artigau É., Marley M., Saumon D., 2012, *ApJ*, **750**, 105

Roche E., 1847, *Mém. Sect. Sci.*, **1**, 243

Rogers T. M., 2017, *Nature Astronomy*, **1**, 0131

Rothman L., et al., 2010, *Journal of Quantitative Spectroscopy and Radiative Transfer*, **111**, 2139

Salz M., Czesla S., Schneider P. C., Schmitt J. H. M. M., 2016, *A&A*, **586**, A75

Schwartz J. C., Cowan N. B., 2017, *PASP*, **129**, 014001

Shporer A., et al., 2019, *AJ*, **157**, 178

Sing D. K., 2010, *A&A*, **510**, A21

Skidmore W., Welsh W. F., Wood J. H., Stiening R. F., 1997, *MNRAS*, **288**, 189

Stevenson K., et al., 2010, *Nature*, **464**, 1161

Stevenson K. B., et al., 2012a, *ApJ*, **754**, 136

Stevenson K. B., et al., 2012b, *ApJ*, **755**, 9

Stevenson K. B., Bean J. L., Seifahrt A., Désert J.-M., Madhusudhan N., Bergmann M., Kreidberg L., Homeier D., 2014a, *AJ*, **147**, 161

Stevenson K. B., Bean J. L., Madhusudhan N., Harrington J., 2014b, *ApJ*, **791**, 36

Stevenson K. B., et al., 2017, *AJ*, **153**, 68

Turner J. D., Christie D., Arras P., Johnson R. E., Schmidt C., 2016, *MNRAS*, **458**, 3880

Vidotto A. A., Jardine M., Helling C., 2010, *ApJL*, **722**, L168

Vidotto A. A., Jardine M., Helling C., 2011, *MNRAS*, **414**, 1573

Welsh W. F., Orosz J. A., Seager S., Fortney J. J., Jenkins J., Rowe J. F., Koch D., Borucki W. J., 2010, *ApJL*, **713**, L145

Winn J. N., et al., 2007, *AJ*, **134**, 1707

Wong I., et al., 2015, *ApJ*, **811**, 122

Wong I., et al., 2016, *ApJ*, **823**, 122

Zellem R. T., et al., 2014, *ApJ*, **790**, 53

Zellem R. T., et al., 2017, *ApJ*, **844**, 27

Zhang M., et al., 2018, *AJ*, **155**, 83

de Wit J., Lewis N. K., Langton J., Laughlin G., Deming D., Batygin K., Fortney J. J., 2016, *ApJL*, **820**, L33

de Wit J., et al., 2017, *ApJL*, **836**, L17

ter Braak C. J. F., Vrugt J. A., 2008, *Statistics and Computing*, **18**, 435

Appendix A: Correction for Dilution by Stellar Companions

To correct for the dilution of our lightcurves by the nearby stellar companions WASP-12BC, we apply the dilution factors from Stevenson et al. (2014a): $\alpha_{\text{comp}} = 0.1149 \pm 0.0039$ and 0.1196 ± 0.0042 for $3.6 \mu\text{m}$ and $4.5 \mu\text{m}$ respectively. Since our phase curve amplitudes are normalized by the eclipse depth, no corrections need to be made to C_1 , D_1 , C_2 , or D_2 . Additionally, while the planetary radii need to be corrected for dilution from WASP-12BC, the ratio $R_{p,2}/R_p$ remains the same for models with ellipsoidal variations. Following Stevenson et al. (2014b,a), the multiplicative correction factor is

$$C_{\text{corr}}(\lambda) = 1 + g(\beta, \lambda) \alpha_{\text{comp}}(\lambda),$$

where $g(\beta, \lambda)$ is the fraction of WASP-12BC's flux which falls within our aperture of size β . We estimated $g(\beta, \lambda)$ using STINYTIM², the point response function modelling software for Spitzer. We made $10\times$ oversampled point response functions calculated at the pixel position (25,25) assuming a $T = 3660$ blackbody source (the effective temperature of WASP-12BC; Stevenson et al. 2014b). We found $g(2.5, 4.5 \mu\text{m}) = 0.8147$, $g(3.2, 4.5 \mu\text{m}) = 0.8608$, $g(4.3, 3.6 \mu\text{m}) = 0.9089$, and $g(2.9, 3.6 \mu\text{m}) = 0.8580$. For the 3×3 pixel stamp used in M. Zhang's PLD analyses, we find $g(3 \times 3, 3.6 \mu\text{m}) = 0.6518$ and $g(3 \times 3, 4.5 \mu\text{m}) = 0.6291$. For P. Cubillo's analyses, we find $g(3.0, 4.5 \mu\text{m}) = 0.8533$, $g(2.5, 4.5 \mu\text{m}) = 0.6957$, $g(2.5, 3.6 \mu\text{m}) = 0.8254$, and $g(4.0, 3.6 \mu\text{m}) = 0.9015$. We also checked $g(2.25, 3.6 \mu\text{m})$ and $g(2.25, 4.5 \mu\text{m})$ to compare our calculation to that of Stevenson et al. (2014b); we find values of 0.8007 and 0.7586, where Stevenson et al. (2014b) found 0.7116 and 0.6931. This discrepancy is likely caused by an incorrect angular separation used in the previous work's calculation.

The planet's radius was then corrected using

$$R_{p,\text{corr}}(\lambda) = \sqrt{C_{\text{corr}}(\lambda)} R_{p,\text{meas}}(\lambda),$$

with the elongated axis, $R_{p,2}$, in bi-axial ellipsoid models corrected similarly. The dayside flux was corrected using

$$F_{\text{day,corr}}(\lambda) = C_{\text{corr}}(\lambda) F_{\text{day,meas}}(\lambda),$$

with the white noise amplitude, σ_F , corrected similarly.

Appendix B: Computing Astrophysical Parameters

Tables A2–A9 present many of the fitted astrophysical values from all models run in all three independent analyses. $T_{b,\text{day}}$ and $T_{b,\text{night}}$ are the apparent brightness temperatures of the planet's day and night hemispheres which we calculate using *only the contribution from the first order sinusoid*. In doing so, we are assuming that the second order sinusoidal variations are attributable to something other than the planet, although the second-order sinusoidal variations end up having negligible contributions during transit and eclipse anyway. These brightness temperatures are calculated by inverting the Planck function (Cowan & Agol 2011),

² <http://irsa.ipac.caltech.edu/data/SPITZER/docs/dataanalysistools/tools/contributed/general/stintym/>

using

$$T_b(\lambda) = \frac{hc}{\lambda k_B} \left[\ln \left(1 + \frac{\exp(hc/\lambda k_B T_{*,\text{b}}) - 1}{\psi(\lambda)} \right) \right]^{-1},$$

where h is Planck's constant, c is the speed of light, k_B is the Boltzmann constant, λ is the wavelength. For $T_{b,\text{day}}$, $\psi = (F_{\text{day}}/F_*)(R_p/R_*)^{-2}$, and for $T_{b,\text{night}}$, $\psi = (F_{\text{day}}/F_*)(1 - 2C_1)(R_p/R_*)^{-2}$. The stellar brightness temperature, $T_{*,\text{b}}$ was calculated by fitting blackbodies to the relevant wavelengths from a PHOENIX stellar model (Husser et al. 2013) with previously measured (Hebb et al. 2009) values of $T_{*,\text{eff}} = 6300$ K and $\log(g) = 4.5$. We find $T_{*,\text{b}} = 6000$ K for $4.5 \mu\text{m}$ and 5800 K for $3.6 \mu\text{m}$. The tabulated first and second order offsets are measured in degrees after the secondary eclipse and are calculated using:

$$\psi_1 = -(180/\pi) \arctan(D_1/C_1)$$

$$\psi_2 = 180 - 0.5(180/\pi) \arctan(D_2/C_2).$$

It is important to note that our reported “eclipse depths” (F_{day}/F_*) are measured with respect to the phase curve value expected at the centre of eclipse and are not measured with respect to pre-ingress and post-egress flux measurements as would be the case for observations of only the eclipse. Given our fitted phase curve parameters for WASP-12b, the difference between our reported value and using the average of pre-ingress and post-egress baselines is $\sim 9\%$ of F_{day}/F_* at both *Spitzer* bandpasses (assuming these baseline durations are both the same duration as the eclipse duration). This bias in eclipse observations occurs because the phase variations before ingress and after egress are flattened out by most decorrelation routines when solely observing the eclipse. For most exoplanets whose phase variations will be concave down around eclipse (like WASP-12b when seen at $3.6 \mu\text{m}$), eclipse observations will underestimate F_{day}/F_* . For the unusual case of WASP-12b's $4.5 \mu\text{m}$ phase variations which are concave up near eclipse, eclipse observations will overestimate F_{day}/F_* . This effect is particularly important for short period planets which undergo significant rotation throughout the duration of eclipse observations and whose strong day–night temperature contrast cause strong phase variations over this time span. Among other things, this may explain the discrepancies between reported $3.6 \mu\text{m}$ and $4.5 \mu\text{m}$ eclipse depths from full-orbit phase curves (Cowan et al. 2012) and eclipse-only observations (Madhusudhan et al. 2011; Stevenson et al. 2014b), and the associated inference of C/O ratio. See Figure A1 for a figure demonstrating this effect.

Appendix C: Tidal Distortion Calculations

To assess the impact of stellar and planetary tidal distortion, we model the stellar/planetary surfaces using the dimensionless Roche potential, defined by

$$\Omega(r, \theta, \phi) = \frac{1}{r} + q \left(\frac{1}{\sqrt{1 - 2r \sin \theta \cos \phi + r^2}} - r \sin \theta \cos \phi \right) + \frac{q+1}{2} r^2 \sin^2 \theta,$$

where r is the distance from the host star, θ is the polar angle, ϕ is the azimuthal angle, and q is the mass ratio,

M_*/M_P . We find that the star's radius should be 0.0085% longer along the star–planet axis compared to the perpendicular equatorial axis, while the planet's radius should be 5.5% longer along the star–planet axis compared to the dawn–dusk axis seen at transit.

We first assume that the planet and star have a constant temperature of 3000 K and 6300 K, respectively, and then perturb these temperatures to account for gravity darkening using the $T_{\text{eff}} \propto g_{\text{eff}}^{\beta}$ model (Espinosa Lara & Rieutord 2011) where β is 0.24 for the appreciably distorted planet and 0.25 for the more spherical host star. Next, we convert these temperature maps into flux maps using the Planck blackbody function. We then compute disk-integrated phase curves (Cowan et al. 2013) while also accounting for the variations in apparent areas of the two objects. Our calculations show that the planet's expected variations are only ~ 3.5 times stronger than that of the host star at *Spitzer*/IRAC wavelengths (see Figure A4 for a depiction).

Our predicted ellipsoidal and gravity darkening variations are consistent with past predictions (Budaj 2011) and with the amplitude of the Zhang PLD model with second order sinusoidal variations fitted to the 3.6 μm data collected in 2010 (we set the offset to zero as there is no significant detection of an offset in this phase curve). However, the expected ellipsoidal and gravity darkening variations are highly discrepant with the observed amplitude at 4.5 μm (see Figure A5). Running simulations where the planet fills its Roche lobe ($R_{p,2}/R_p \approx 1.4$), our ellipsoidal variations and gravity darkening model would be able to explain the full amplitude of the 4.5 μm phase curve, but the variations remain mostly monochromatic and the model drastically over predicts the variations in the 3.6 μm phase curve.

Appendix D: Red Noise Tests

The bottom rows of Figures A6–A11 show the observed standard deviation in the residuals versus the number of data cubes binned together for each lightcurve made using the `binrms` routine from the Multi-Core Markov-Chain Monte Carlo (MC3)³ package (Cubillos et al. 2017); this allows us to test for any red noise remaining in our residuals (Winn et al. 2007; Cowan et al. 2012). These figures show that minimal red noise remains after our fiducial models have been subtracted from the data (the photometric uncertainty decays roughly as $\sqrt{N_{\text{binned}}}$). There is, however, some lower-frequency noise in the 2010 4.5 μm observations between the first eclipse and the transit that cannot be modelled by any of the three decorrelation pipelines.

Appendix E: NUV Evidence for Mass Loss

Across the NUV, WASP-12b appears to be larger than the planet's Roche radius, implying significant mass loss (Fossati et al. 2010; Haswell et al. 2012; Nichols et al. 2015). The first Hubble Space Telescope, Cosmic Origins Spectrograph transit observation of WASP-12b (Fossati et al. 2010) also detected an early ingress in the NUV; this suggests the presence of a stream of gas stripped from the planet flowing in toward the star (Lai et al. 2010; Bisikalo et al. 2013b; Matsakos

et al. 2015) which forms a bow shock ahead of the planet (Vidotto et al. 2010; Llama et al. 2011; Bisikalo et al. 2013b; Cherenkov et al. 2014; Matsakos et al. 2015; Turner et al. 2016). There is also evidence for variable NUV ingress times (Haswell et al. 2012; Nichols et al. 2015) which suggests variable mass-loss rates and/or a variations in the planet–shock distance (Vidotto et al. 2011). The non-detection of stellar activity indicators from WASP-12A (Knutson et al. 2010; Fossati et al. 2013) may also suggest that WASP-12b is undergoing mass loss. The final resting place of the gas stripped from WASP-12b is debated, with some suggesting an accretion disk interior to the planet's orbit (Lai et al. 2010; Li et al. 2010) and others suggesting an extended circumstellar torus of gas with the planet embedded inside (Debrecht et al. 2018).

Appendix F: Discussion of Variability

To date, no *Spitzer* phase curve observation has shown variability in the phase curve offset of an exoplanet, although significant near-infrared variability has been seen for brown dwarfs and isolated planetary mass objects (Artigau et al. 2009; Radigan et al. 2012), and *Kepler* phase curves of the hot Jupiter HAT-P-7b have been reported to vary (Armstrong et al. 2016). Variability is expected for WASP-12b due to coupling between the planet's partially ionized atmosphere and the planet's magnetic field (Rogers 2017). The timescale of this variability is set by the Alfvén timescale (~ 115 days for WASP-12b assuming magnetic effects occur on the dayside where the atmosphere is dominated by atomic hydrogen; Rogers 2017; Dang et al. 2018). Variability may also arise in the presence of time-variable cloud coverage, although optically reflective clouds on the planet's dayside were stringently rejected using *Hubble*/STIS optical eclipse spectroscopy of WASP-12b (Bell et al. 2017). Any time-variability in the gas streaming from the planet could also obscure different portions of the planet over time and lead to an apparent variation in the 3.6 μm phase curve.

Appendix G: Model Selection

The preferred model for each phase curve was chosen to be the model with the lowest Bayesian Information Criterion (BIC), defined as

$$\text{BIC} = -2 \ln(L) + N_{\text{par}} \ln(N_{\text{dat}}),$$

where N_{par} is the number of model parameters and N_{dat} is the number of data. The log-likelihood is

$$\ln(L) = -\frac{\chi^2}{2} - N_{\text{dat}} \ln(\sigma_F) - \frac{N_{\text{dat}}}{2} \ln(2\pi)$$

where σ_F is the fitted photometric uncertainty (assumed to be constant throughout the observation) and

$$\chi^2 = \frac{\sum_i (F_{\text{obs},i} - F_{\text{model},i})^2}{\sigma_F^2}$$

is a measure of the badness-of-fit, where $F_{\text{obs},i}$ are the observed flux measurements. We adopt the threshold that models with a $\Delta\text{BIC} \leq 5$ with respect to the favoured model cannot be strongly ruled out.

³ <http://pcubillos.github.io/MCcubed/>

Table A1. 3.6 and 4.5 μm phase curve parameters from the preferred models for 2010 and 2013. Fiducial models are indicated with bolding.**3.6 μm**

Data Set	Model	C_1	D_1	C_2	D_2	F_{day}/F_* \dagger (ppm)	$\frac{\ln(L)}{N_{\text{data}}}$ \dagger
2010	A1, Poly4, 2nd Order	0.436 ± 0.033	-0.067 ± 0.061	0.027 ± 0.028	0.076 ± 0.022	3840 ± 210	5.2
2010	A2, PLD, 1st Order	0.371 ± 0.051	-0.239 ± 0.046			3870 ± 130	5.62
2010	A3, BLISS, 1st Order	0.395 ± 0.036	-0.237 ± 0.036			3780 ± 120	3.65
2013	A1, Poly3*f(t), 1st Order	0.299 ± 0.029	0.105 ± 0.030			3970 ± 150	5.37
2013	A2, PLD, 1st Order	0.320 ± 0.024	0.079 ± 0.025			3840 ± 120	5.6
2013	A3, BLISS, 1st Order	0.324 ± 0.024	0.091 ± 0.023			3810 ± 120	3.59

3.6 μm , cont.

Data Set	Model	R_p/R_* \ddagger	Phase Offset (degrees)		$T_{b,\text{day}}$ \dagger (K)	$T_{b,\text{night}}$ \dagger (K)	$\frac{\ln(L)}{N_{\text{data}}}$ \dagger
			1st Order \dagger	2nd Order \dagger			
2010	A1, Poly4, 2nd Order	0.1197 ± 0.0012	-8.8 ± 7.9	144.7 ± 9.6	2655 ± 76	1190 ± 180	5.2
2010	A2, PLD, 1st Order	0.11642 ± 0.00063	-32.6 ± 6.2		2744 ± 48	1510 ± 210	5.62
2010	A3, BLISS, 1st Order	0.11782 ± 0.00096	-30.9 ± 4.5		2603 ± 49	1360 ± 160	3.65
2013	A1, Poly3*f(t), 1st Order	0.1159 ± 0.0011	19.3 ± 4.3		2795 ± 64	1830 ± 110	5.37
2013	A2, PLD, 1st Order	0.11327 ± 0.00068	13.6 ± 3.8		2813 ± 48	1760 ± 97	5.60
2013	A3, BLISS, 1st Order	0.1169 ± 0.0011	15.7 ± 4.0		2637 ± 47	1658 ± 83	3.59

4.5 μm

Data Set	Model	C_1	D_1	C_2	D_2	F_{day}/F_* \dagger (ppm)	$\frac{\ln(L)}{N_{\text{data}}}$ \dagger
2010	A1, BLISS, 2nd Order	0.414 ± 0.044	-0.218 ± 0.054	-0.265 ± 0.037	0.031 ± 0.025	4200 ± 200	5.22
2010	A2, PLD, 2nd Order	0.489 ± 0.016	-0.080 ± 0.020	-0.252 ± 0.019	0.042 ± 0.014	4360 ± 140	5.45
2010	A3, BLISS, 2nd Order	0.476 ± 0.030	-0.137 ± 0.030	-0.263 ± 0.027	0.043 ± 0.017	4380 ± 170	3.37
2013	A1, BLISS, 2nd Order	0.271 ± 0.053	-0.096 ± 0.046	-0.303 ± 0.043	0.122 ± 0.034	3920 ± 210	5.22
2013	A2, PLD, 2nd Order	0.395 ± 0.036	-0.136 ± 0.025	-0.307 ± 0.023	0.034 ± 0.021	3920 ± 150	5.43
2013	A3, BLISS, 2nd Order	0.376 ± 0.030	-0.091 ± 0.027	-0.292 ± 0.029	0.041 ± 0.020	4120 ± 160	3.41

4.5 μm , cont.

Data Set	Model	R_p/R_* \ddagger	Phase Offset (degrees)		$T_{b,\text{day}}$ \dagger (K)	$T_{b,\text{night}}$ \dagger (K)	$\frac{\ln(L)}{N_{\text{data}}}$ \dagger
			1st Order \dagger	2nd Order \dagger			
2010	A1, BLISS, 2nd Order	0.1078 ± 0.0013	-27.9 ± 6.1	93.4 ± 2.7	2879 ± 91	1250 ± 240	5.22
2010	A2, PLD, 2nd Order	0.10656 ± 0.00085	-9.5 ± 2.3	94.7 ± 1.6	2989 ± 66	790 ± 150	5.45
2010	A3, BLISS, 2nd Order	0.1075 ± 0.0014	-16.0 ± 3.5	94.6 ± 1.9	2965 ± 78	940 ± 210	3.37
2013	A1, BLISS, 2nd Order	0.1092 ± 0.0016	-19 ± 11	100.9 ± 3.1	2722 ± 92	1800 ± 200	5.22
2013	A2, PLD, 2nd Order	0.1049 ± 0.0010	-19.1 ± 3.9	93.2 ± 1.9	2854 ± 74	1340 ± 180	5.43
2013	A3, BLISS, 2nd Order	0.1104 ± 0.0014	-13.6 ± 4.0	94.0 ± 1.9	2768 ± 73	1400 ± 140	3.41

[†] These are derived quantities and are not fitted directly.[‡] These quantities have been corrected for dilution from WASP-12BC (see supplementary text).

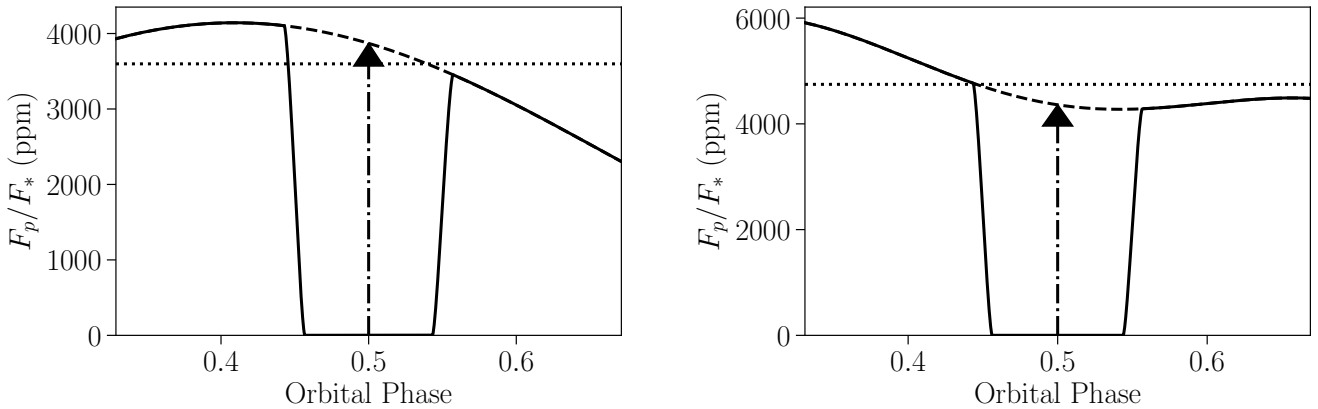


Figure A1. Bias present in eclipse-only observations of exoplanets. *Left:* Our fiducial model for the 2010 phase curve at 3.6 μm is shown with a solid line, while the model neglecting the secondary eclipse is shown with a dashed line. It is with respect to this line that we calculate our eclipse depth (shown with a dash-dotted arrow), while the eclipse depth that would be measured using eclipse-only observations is shown with a dotted line. This bias occurs because there is insufficient evidence of phase variations with eclipse-only observations, so a flat or a sloped line is used instead. *Right:* The same bias at 4.5 μm but in the opposite direction due to the abnormal concave-up phase variations near the 4.5 μm eclipse.

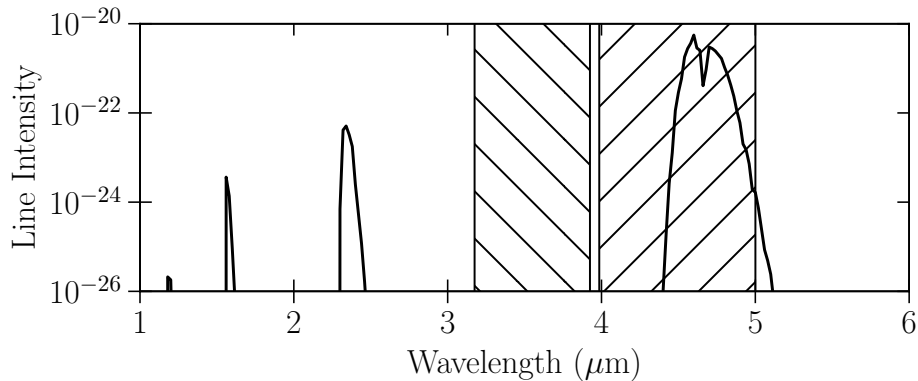


Figure A2. CO line intensities at 296 K from HITEMP (Rothman et al. 2010) in units of $\text{cm}^{-1}/(\text{molecule} \times \text{cm}^{-2})$ which has been binned to a spectral resolution of 10 cm. The bandwidths of *Spitzer*/IRAC channels 1 and 2 are respectively shown with downward sloping and upward sloping hatched regions.

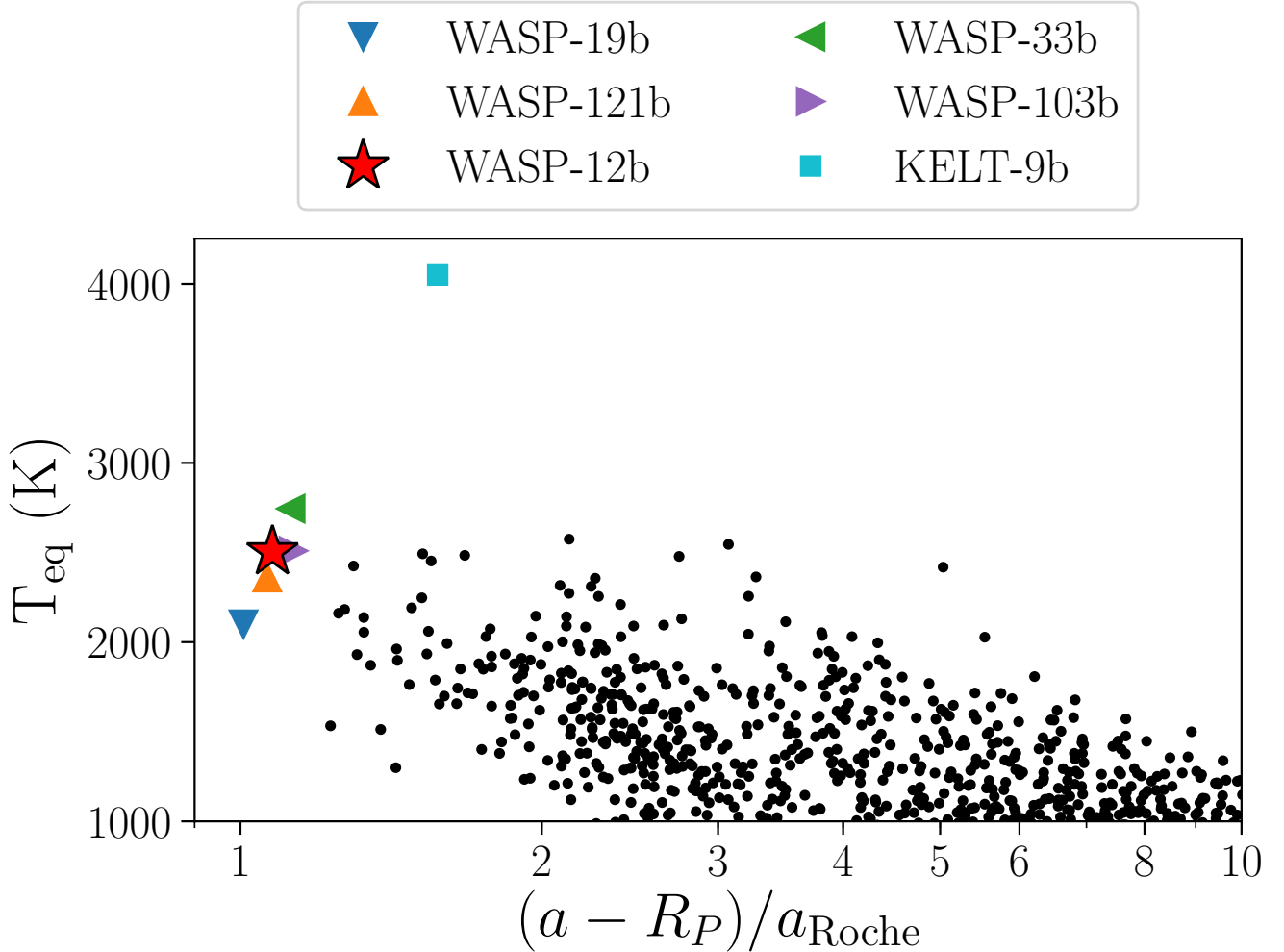


Figure A3. A comparison of WASP-12b to other exoplanets. The y-axis is the planets' equilibrium temperature ($T_{\text{eq}} = 0.25^{0.25} T_* \sqrt{R_*/a}$), and this x-axis is the distance of the substellar point on the planets from their L1 Lagrange point (Roche 1847), where $a_{\text{Roche}} = 2.44(R_p)(M_*/M_p)^{1/3}$. While WASP-12b is one of the exoplanets closest to overflowing its Roche lobe, there are several others with similar characteristics for which Spitzer phase curves do not show strong second order sinusoidal variations at 4.5 μm (Wong et al. 2016; Zhang et al. 2018; Kreidberg et al. 2018). One potential explanation is that WASP-12b's orbit may be decaying (Maciejewski et al. 2016; Patra et al. 2017) while the other exoplanets may be more stable.

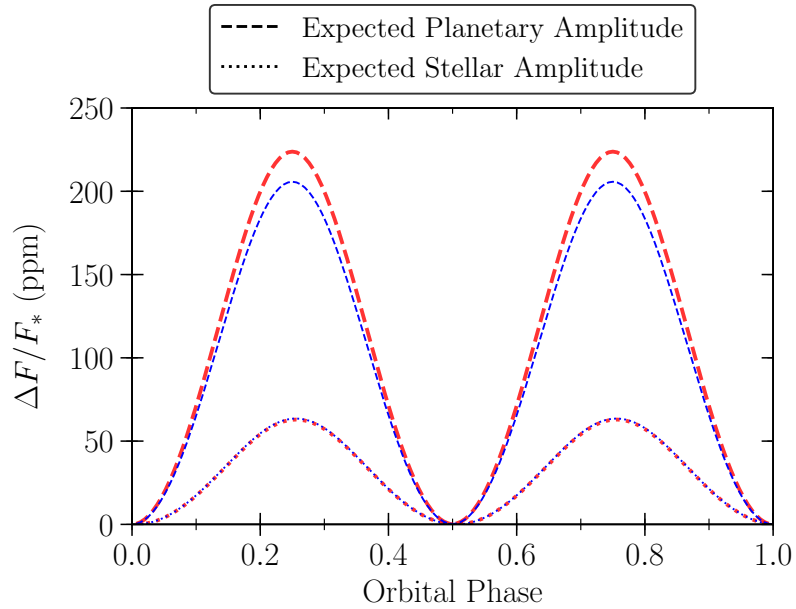


Figure A4. Expected amplitude of tidal distortion from the host star compared to that from the planet. Thin blue lines show the amplitudes at $3.6\ \mu\text{m}$, while thick red lines show the amplitudes at $4.5\ \mu\text{m}$.

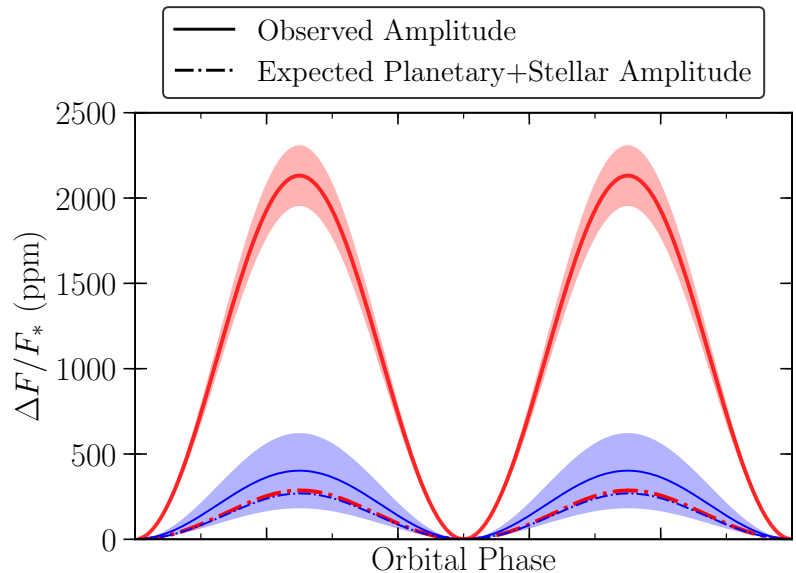


Figure A5. Observed second order sinusoidal variations at $3.6\ \mu\text{m}$ and $4.5\ \mu\text{m}$ and their 1σ uncertainties compared to the expected amplitude of tidal distortion from the host star and the planet. The $3.6\ \mu\text{m}$ phase curve is consistent with the expected amplitudes while the $4.5\ \mu\text{m}$ phase curve is highly discrepant. Thin blue lines show the amplitudes at $3.6\ \mu\text{m}$, while thick red lines show the amplitudes at $4.5\ \mu\text{m}$.

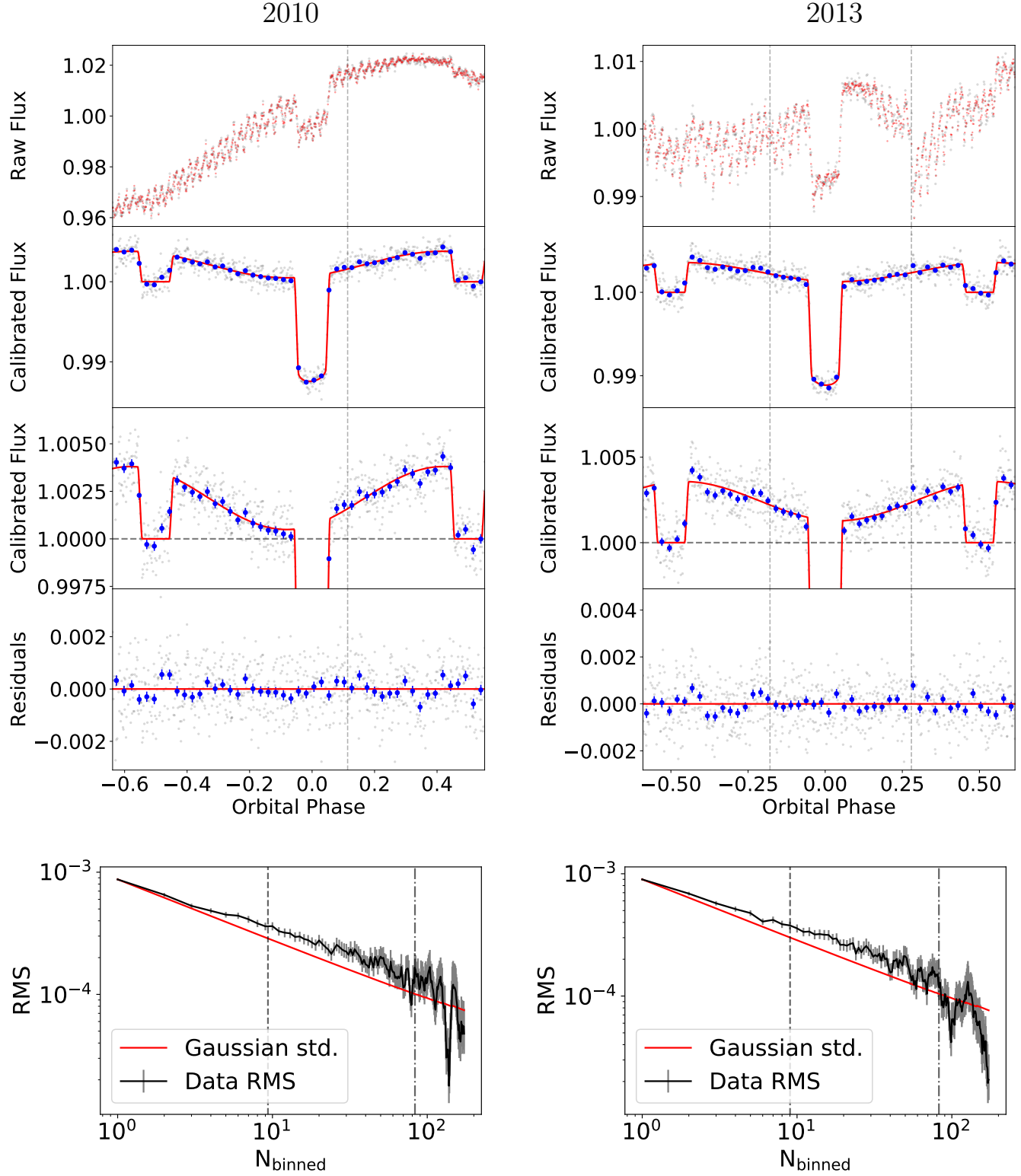


Figure A6. Top row: WASP-12b 2010 (left) and 2013 (right) $3.6\text{ }\mu\text{m}$ observations, fit using the Zhang PLD detector model and second- (2010) and first order (2013) phase variations model. Vertical dashed lines mark the transitions between AORs. Bottom row: Red noise test for the 2010 (left) and 2013 (right) $3.6\text{ }\mu\text{m}$ observations of WASP-12b for the above fits. The black line shows the decrease in the observed standard deviation in the residuals as N_{binned} (the number of datapoints binned together) increases. The red line shows the expected decrease in standard deviation, assuming the noise is entirely white. The close match between the two curves suggests that little-to-no red-noise remains in the residuals. A vertical, dashed line shows the timescale for transit/eclipse ingress and egress, while the dash-dotted line shows the t_1-t_4 transit duration.

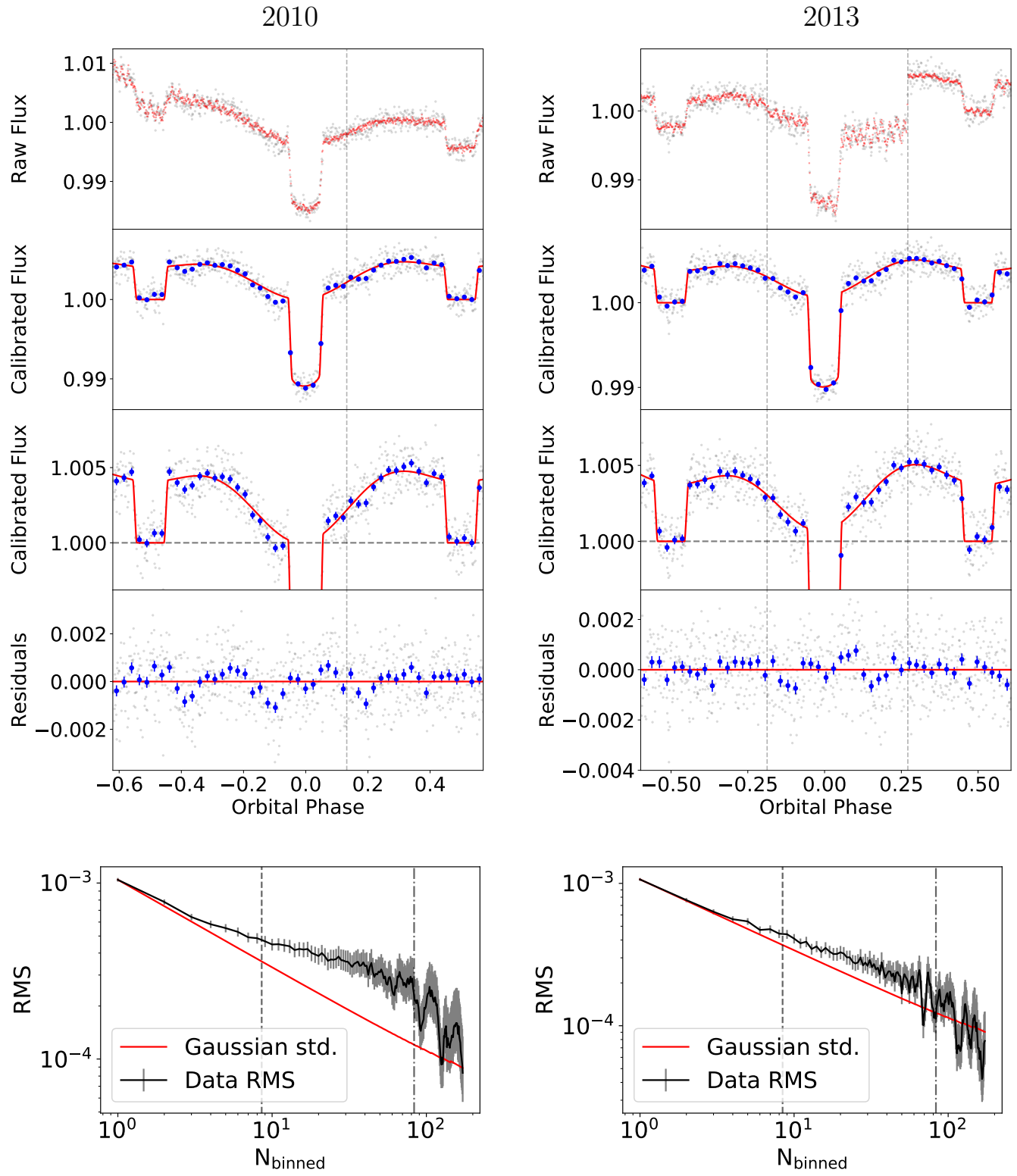


Figure A7. Same figure as the left panel of Figure A6 but for the 2010 (left column) and 2013 (right column) 4.5 μm observations of WASP-12b, both fit using the Zhang PLD detector model and the second order phase variations model.

Supplementary Information

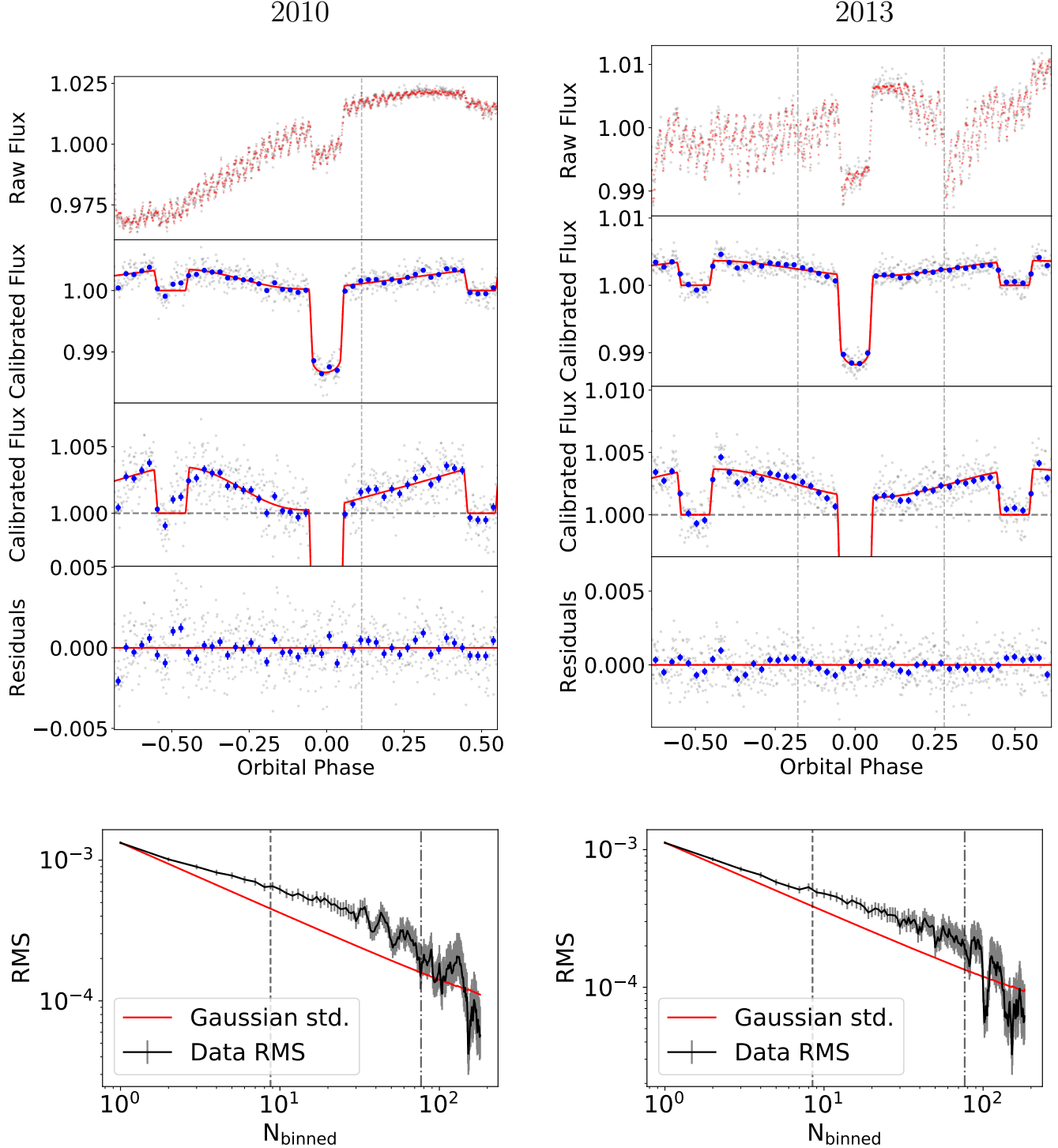


Figure A8. Same as Figure A6 but for the 2010 (left) and 2013 (right) $3.6\ \mu\text{m}$ observations of WASP-12b, fit using the SPCA Poly4 (2010) and SPCA Poly3* $f(t)$ (2013) detector models and the second- (2010) and first order (2013) phase variations model.

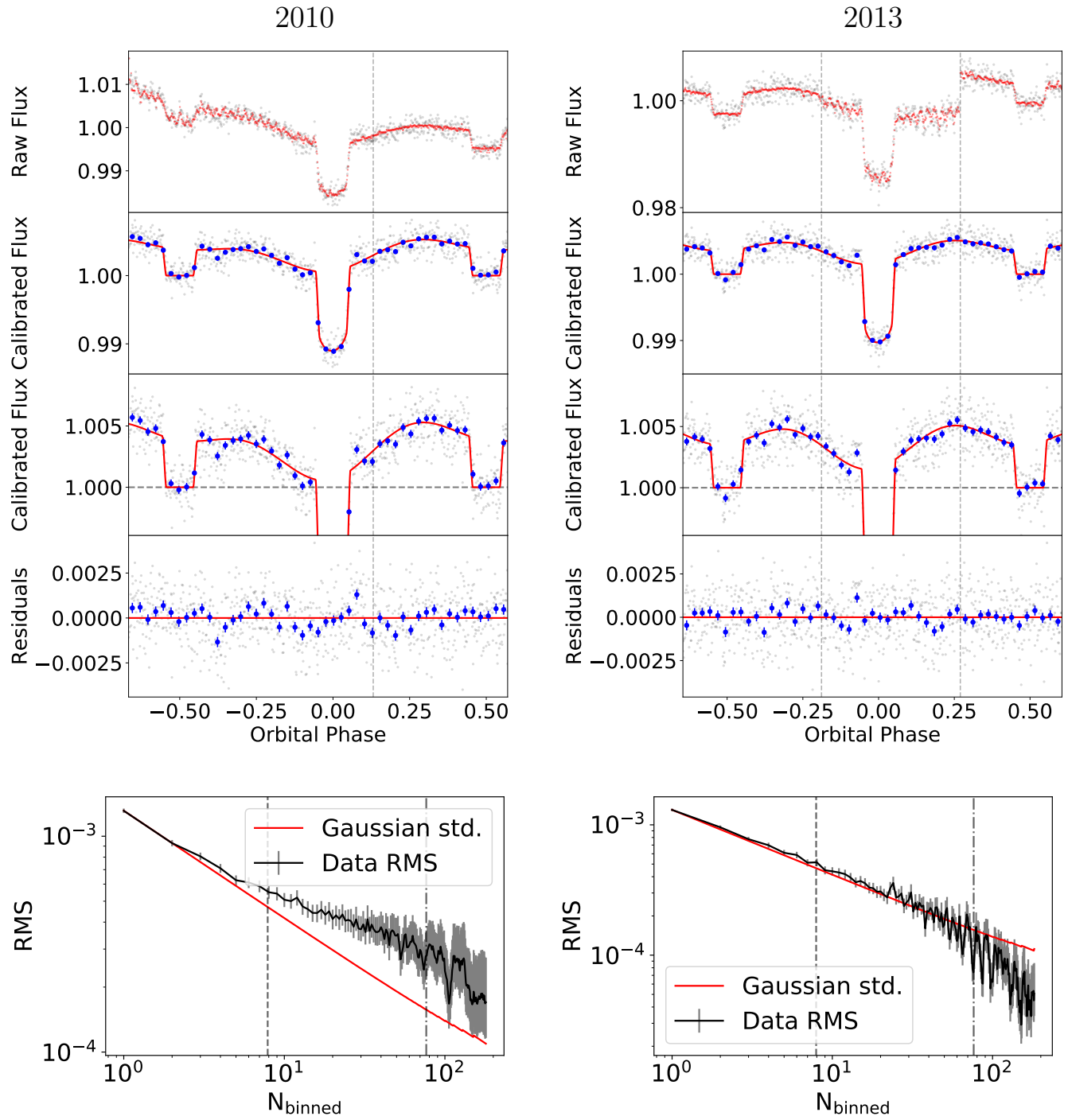


Figure A9. Same figure as Figure A6 but for the 2010 (left) and 2013 (right) 4.5 μm observations of WASP-12b, both fit using the SPCA BLISS detector model and the second order phase variations model.

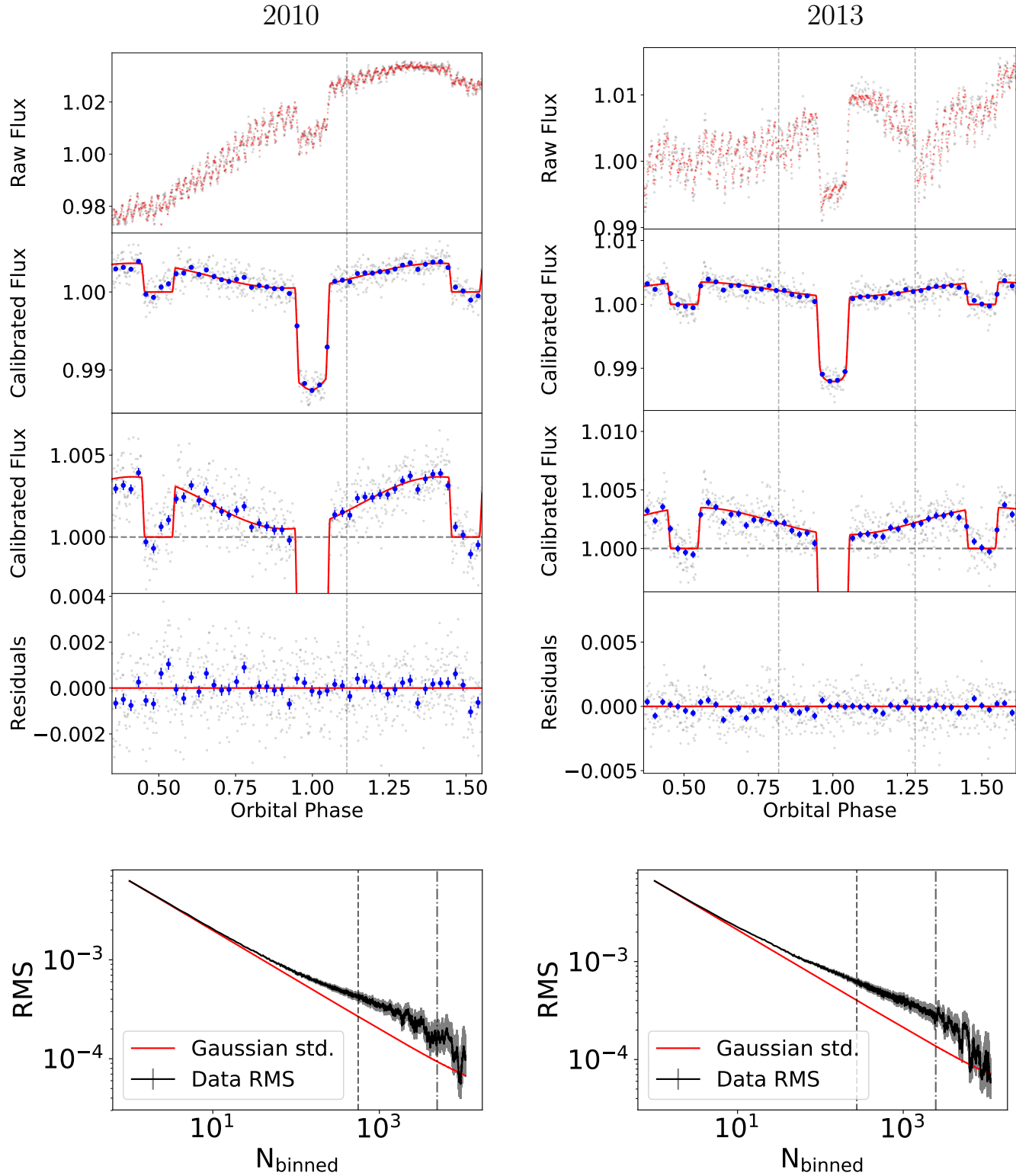


Figure A10. Same figure as Figure A6 but for the 2010 (left) and 2013 (right) 3.6 μm observations of WASP-12b, both fit using the POET pipeline.

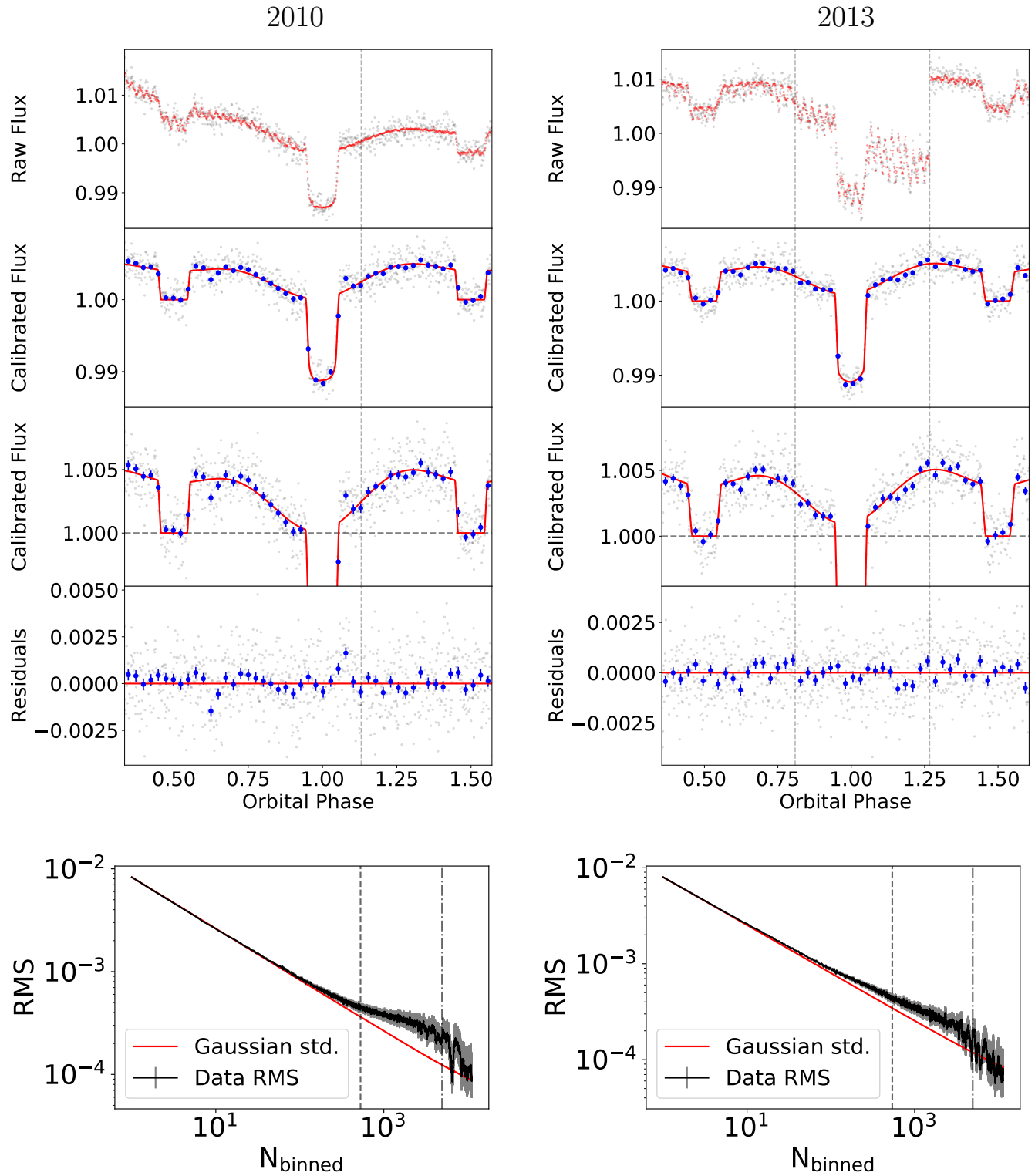


Figure A11. Same figure as Figure A6 but for the 2010 (left) and 2013 (right) 4.5 μm observations of WASP-12b, both fit using the POET pipeline.

Supplementary Table 2: Best-fit 3.6 μm Phase Curve Parameters from 2010. A1, A2, and A3 refer to the independent Analyses 1–3.

Detector Model	Astrophysical Model	C_1	D_1	C_2	D_2	F_{day}/F_* [†] (ppm)	σ_F [‡] (ppm)	χ^2	$\Delta\text{BIC}^{\dagger a}$
A1,Poly2	1st Order	-0.553 ± 0.064	-0.850 ± 0.074			4460 ± 270	2274 ± 53	907.9	716
A1,Poly2	2nd Order	-0.573 ± 0.073	-0.874 ± 0.088	-0.016 ± 0.039	-0.004 ± 0.029	4340 ± 330	2276 ± 55	906.58	730
A1,Poly2	1st Order + Ellipse	-0.551 ± 0.067	-0.852 ± 0.079			4460 ± 290	2275 ± 53	907.42	723
A1,Poly3	1st Order	0.308 ± 0.027	-0.603 ± 0.042			3810 ± 160	1648 ± 39	900.38	155
A1,Poly3	2nd Order	0.265 ± 0.028	-0.528 ± 0.046	0.035 ± 0.024	0.091 ± 0.022	4140 ± 220	1634 ± 39	896.46	149
A1,Poly3	1st Order + Ellipse	0.298 ± 0.027	-0.621 ± 0.042			4180 ± 210	1645 ± 39	896.58	154
A1,Poly4	1st Order	0.453 ± 0.038	-0.064 ± 0.067			3620 ± 170	1493 ± 35	889.85	0
A1,Poly4	2nd Order	0.436 ± 0.033	-0.067 ± 0.061	0.027 ± 0.028	0.076 ± 0.022	3840 ± 210	1484 ± 35	887.37	0
A1,Poly4	1st Order + Ellipse	0.461 ± 0.028	-0.126 ± 0.074			3890 ± 210	1493 ± 36	885.35	3
A1,Poly5	1st Order	0.415 ± 0.064	-0.055 ± 0.074			3490 ± 200	1481 ± 34	885.42	26
A1,Poly5	2nd Order	0.418 ± 0.048	-0.070 ± 0.064	0.037 ± 0.030	0.064 ± 0.024	3720 ± 210	1473 ± 33	888.5	34
A1,Poly5	1st Order + Ellipse	0.429 ± 0.047	-0.175 ± 0.089			3740 ± 230	1477 ± 35	882.2	26
A1,BLISS	1st Order	0.374 ± 0.059	-0.235 ± 0.070			4280 ± 240	1792 ± 43	901.76	244
A1,BLISS	2nd Order	0.366 ± 0.054	-0.248 ± 0.065	0.032 ± 0.037	0.021 ± 0.032	4420 ± 270	1793 ± 42	899.5	256
A1,BLISS	1st Order + Ellipse	0.381 ± 0.048	-0.326 ± 0.079			4550 ± 270	1786 ± 42	902.16	245
A2,PLD	1st Order	0.371 ± 0.051	-0.239 ± 0.046			3870 ± 130	950 ± 23	865.0	0
A2,PLD	2nd Order	0.374 ± 0.047	-0.222 ± 0.045	0.025 ± 0.018	0.038 ± 0.014	3990 ± 150	946 ± 23	865.07	4
A2,PLD	1st Order + Ellipse	0.367 ± 0.052	-0.234 ± 0.047			3840 ± 130	952 ± 23	865.01	8
A3,BLISS	1st Order	0.395 ± 0.036	-0.237 ± 0.036			3780 ± 120	6915 ± 87	54053	0
A3,BLISS	2nd Order	0.399 ± 0.037	-0.253 ± 0.037	-0.015 ± 0.022	0.048 ± 0.020	3790 ± 140	6915 ± 87	54047	18
A3,BLISS	1st Order + Ellipse	0.397 ± 0.036	-0.275 ± 0.041			4040 ± 290	6915 ± 87	54049	15

[†]These are derived quantities and are not fitted directly.

[‡]These quantities have been corrected for dilution from WASP-12BC (see supplementary text).

^a ΔBIC is defined from the preferred model from each analysis pipeline.

Supplementary Table 3: Best-fit 3.6 μm Phase Curve Parameters from 2013. A1, A2, and A3 refer to the independent Analyses 1–3.

Detector Model	Astrophysical Model	C_1	D_1	C_2	D_2	$F_{\text{day}}/F_{*}^{\dagger}$ (ppm)	σ_F^{\dagger} (ppm)	χ^2	ΔBIC^a
A1,Poly2	1st Order	0.419 \pm 0.023	0.159 \pm 0.028			4430 \pm 180	1527 \pm 36	900.39	342
A1,Poly2* $f(t)$	1st Order	0.208 \pm 0.026	0.010 \pm 0.029			3900 \pm 160	1327 \pm 31	899.48	93
A1,Poly2* $f(t)$	2nd Order	0.209 \pm 0.030	-0.046 \pm 0.032	-0.058 \pm 0.036	0.168 \pm 0.024	3740 \pm 170	1290 \pm 30	896.13	52
A1,Poly2* $f(t)$	1st Order + Ellipse	0.209 \pm 0.028	0.012 \pm 0.031			3900 \pm 180	1328 \pm 32	897.58	100
A1,Poly3*$f(t)$	1st Order	0.299 \pm 0.029	0.105 \pm 0.030			3970 \pm 150	1246 \pm 29	893.46	0
A1,Poly3* $f(t)$	2nd Order	0.317 \pm 0.042	0.092 \pm 0.037	-0.036 \pm 0.039	0.018 \pm 0.030	3870 \pm 170	1247 \pm 30	891.96	13
A1,Poly3* $f(t)$	1st Order + Ellipse	0.299 \pm 0.032	0.108 \pm 0.031			3970 \pm 180	1246 \pm 29	893.65	7
A1,Poly4* $f(t)$	1st Order	0.302 \pm 0.031	0.108 \pm 0.033			3970 \pm 150	1246 \pm 30	888.32	29
A1,Poly4* $f(t)$	2nd Order	0.313 \pm 0.043	0.074 \pm 0.046	-0.053 \pm 0.043	0.029 \pm 0.033	3840 \pm 180	1246 \pm 29	887.08	41
A1,Poly4* $f(t)$	1st Order + Ellipse	0.301 \pm 0.034	0.106 \pm 0.036			3970 \pm 170	1247 \pm 29	888.07	36
A1,Poly5* $f(t)$	1st Order	0.276 \pm 0.036	0.086 \pm 0.036			3950 \pm 150	1244 \pm 29	883.38	65
A1,Poly5* $f(t)$	2nd Order	0.281 \pm 0.049	0.051 \pm 0.046	-0.045 \pm 0.044	0.033 \pm 0.036	3830 \pm 180	1244 \pm 30	884.77	80
A1,Poly5* $f(t)$	1st Order + Ellipse	0.270 \pm 0.038	0.089 \pm 0.036			3970 \pm 180	1243 \pm 29	884.16	71
A1,BLISS* $f(t)$	1st Order	0.4683 \pm 0.0082	0.219 \pm 0.024			4440 \pm 180	1504 \pm 35	904.44	288
A1,BLISS* $f(t)$	2nd Order	0.484 \pm 0.012	0.108 \pm 0.045	-0.165 \pm 0.038	0.142 \pm 0.034	3930 \pm 190	1478 \pm 35	903.4	269
A1,BLISS* $f(t)$	1st Order + Ellipse	0.4751 \pm 0.0078	0.188 \pm 0.025			4090 \pm 230	1500 \pm 35	901.6	287
A2,PLD	1st Order	0.320 \pm 0.024	0.079 \pm 0.025			3840 \pm 120	976 \pm 24	866.03	0
A2,PLD	2nd Order	0.349 \pm 0.028	0.073 \pm 0.027	-0.038 \pm 0.027	-0.021 \pm 0.021	3770 \pm 130	975 \pm 23	866.06	12
A2,PLD	1st Order + Ellipse	0.326 \pm 0.024	0.070 \pm 0.025			3760 \pm 130	976 \pm 24	866.0	8
A3,BLISS	1st Order	0.324 \pm 0.024	0.091 \pm 0.023			3810 \pm 120	7360 \pm 90	56764	0
A3,BLISS	2nd Order	0.331 \pm 0.032	0.052 \pm 0.029	-0.052 \pm 0.027	0.050 \pm 0.023	3680 \pm 130	7361 \pm 90	56756	28
A3,BLISS	1st Order + Ellipse	0.296 \pm 0.029	0.046 \pm 0.038			4010 \pm 240	7361 \pm 90	56762	31

[†]These are derived quantities and are not fitted directly.

[‡]These quantities have been corrected for dilution from WASP-12BC (see supplementary text).

^a ΔBIC is defined from the preferred model from each analysis pipeline.

Supplementary Table 4: Best-fit 3.6 μm Planetary Parameters from 2010. A1, A2, and A3 refer to the independent Analyses 1–3.

Detector Model	Astrophysical Model	Phase Offset (degrees)				$T_{b,\text{night}}^{\dagger}$	$\Delta\text{BIC}^{\ddagger a}$
		R_p/R_*^{\ddagger}	$R_{p,2}/R_*^{\ddagger}$	1st Order [†]	2nd Order [†]		
A1,Poly2	1st Order	0.1221 \pm 0.0016		-123.1 \pm 3.2		2810 \pm 100	4380 \pm 140
A1,Poly2	2nd Order	0.1219 \pm 0.0017		-123.1 \pm 3.1	263 \pm 51	2780 \pm 110	4360 \pm 150
A1,Poly2	1st Order + Ellipse	0.1222 \pm 0.0018	0.996 \pm 0.044	-122.7 \pm 3.4		2810 \pm 100	4370 \pm 140
A1,Poly3	1st Order	0.1207 \pm 0.0012		-62.9 \pm 3.6		2625 \pm 69	1710 \pm 83
A1,Poly3	2nd Order	0.1213 \pm 0.0013		-63.2 \pm 3.8	145.6 \pm 7.0	2723 \pm 78	1910 \pm 95
A1,Poly3	1st Order + Ellipse	0.1216 \pm 0.0013	0.1029 \pm 0.0064	0.846 \pm 0.056	-64.3 \pm 3.6	2729 \pm 77	1797 \pm 92
A1,Poly4	1st Order	0.1194 \pm 0.0012		-8.1 \pm 8.5		2586 \pm 70	1080 \pm 230
A1,Poly4	2nd Order	0.1197 \pm 0.0012		-8.8 \pm 7.9	144.7 \pm 9.6	2655 \pm 76	1190 \pm 180
A1,Poly4	1st Order + Ellipse	0.1198 \pm 0.0012	0.10 \pm 0.010	0.830 \pm 0.093	-15.3 \pm 8.6	2671 \pm 79	1050 \pm 180
A1,Poly5	1st Order	0.1189 \pm 0.0012		-8 \pm 10		2547 \pm 76	1270 \pm 300
A1,Poly5	2nd Order	0.1194 \pm 0.0012		-9.5 \pm 8.6	150 \pm 11	2622 \pm 78	1280 \pm 230
A1,Poly5	1st Order + Ellipse	0.1196 \pm 0.0012	0.090 \pm 0.011	0.749 \pm 0.098	-23 \pm 11	2625 \pm 85	1220 \pm 230
A1,BLISS	1st Order	0.1196 \pm 0.0015		-32.6 \pm 8.5		2814 \pm 91	1530 \pm 260
A1,BLISS	2nd Order	0.1197 \pm 0.0016		-34.4 \pm 8.3	163 \pm 25	2860 \pm 100	1590 \pm 230
A1,BLISS	1st Order + Ellipse	0.1199 \pm 0.0016	0.094 \pm 0.011	0.781 \pm 0.092	-40.9 \pm 8.1	2902 \pm 100	1540 \pm 220
A2,PLD	1st Order	0.11642 \pm 0.00063		-32.6 \pm 6.2		2741 \pm 54	1530 \pm 220
A2,PLD	2nd Order	0.11693 \pm 0.00072		-30.6 \pm 6.2	152 \pm 11	2782 \pm 57	1530 \pm 190
A2,PLD	1st Order + Ellipse	0.11635 \pm 0.00063	0.1180 \pm 0.0019	1.014 \pm 0.023	-32.4 \pm 6.3	2736 \pm 50	1550 \pm 210
A3,BLISS	1st Order	0.11782 \pm 0.00096		-30.9 \pm 4.5		2603 \pm 46	1390 \pm 150
A3,BLISS	2nd Order	0.11776 \pm 0.00098		-32.4 \pm 4.5	126 \pm 13	2604 \pm 53	1360 \pm 160
A3,BLISS	1st Order + Ellipse	0.11790 \pm 0.00096	0.92 \pm 0.17	7.8 \pm 2.5	-34.7 \pm 4.7	2700 \pm 110	1390 \pm 170

[†]These are derived quantities and are not fitted directly.

[‡]These quantities have been corrected for dilution from WASP-12BC (see supplementary text).

^a ΔBIC is defined from the preferred model from each analysis pipeline.

Supplementary Table 5: Best-fit 3.6 μm Planetary Parameters from 2013. A1, A2, and A3 refer to the independent Analyses 1–3.

Detector Model	Astrophysical Model	Phase Offset (degrees)			$T_{b,\text{night}}^{\dagger}$	$T_{b,\text{day}}^{\dagger}$	ΔBIC^a
		R_p/R_*	$R_{p,2}/R_*$	$R_{p,2}/R_p$			
A1,Poly2	1st Order	0.1151 \pm 0.0013			20.7 \pm 3.1	3086 \pm 96	1400 \pm 130
A1,Poly2*f(t)	1st Order	0.1166 \pm 0.0012			2.7 \pm 7.7	2753 \pm 67	2117 \pm 79
A1,Poly2*f(t)	2nd Order	0.1164 \pm 0.0012			-12.4 \pm 9.0	125.5 \pm 5.7	2696 \pm 68
A1,Poly2*f(t)	1st Order + Ellipse	0.1166 \pm 0.0012	0.1161 \pm 0.0090	0.996 \pm 0.080	3.4 \pm 8.3	2752 \pm 71	2080 \pm 100
A1,Poly3*f(t)	1st Order	0.1159 \pm 0.0011			19.3 \pm 4.3	2795 \pm 64	2116 \pm 91
A1,Poly3*f(t)	2nd Order	0.1154 \pm 0.0012			16.0 \pm 5.8	103 \pm 23	1830 \pm 110
A1,Poly3*f(t)	1st Order + Ellipse	0.1161 \pm 0.0011	0.1147 \pm 0.0094	0.988 \pm 0.084	19.6 \pm 4.9	2789 \pm 69	1750 \pm 160
A1,Poly4*f(t)	1st Order	0.1163 \pm 0.0012			19.6 \pm 4.9	2787 \pm 62	1820 \pm 120
A1,Poly4*f(t)	2nd Order	0.1159 \pm 0.0012			13.2 \pm 7.4	105 \pm 17	1810 \pm 110
A1,Poly4*f(t)	1st Order + Ellipse	0.1163 \pm 0.0012	0.1156 \pm 0.0095	0.994 \pm 0.086	19.3 \pm 5.4	2786 \pm 69	1750 \pm 160
A1,Poly5*f(t)	1st Order	0.1161 \pm 0.0012			17.5 \pm 5.6	2785 \pm 63	1810 \pm 130
A1,Poly5*f(t)	2nd Order	0.1158 \pm 0.0013			10.3 \pm 8.6	108 \pm 20	1745 \pm 69
A1,Poly5*f(t)	1st Order + Ellipse	0.1161 \pm 0.0012	0.1130 \pm 0.0099	0.973 \pm 0.091	18.2 \pm 6.3	2786 \pm 69	1810 \pm 130
A1,BLISS*f(t)	1st Order	0.1169 \pm 0.0014			25.0 \pm 2.5	2945 \pm 82	1910 \pm 130
A1,BLISS*f(t)	2nd Order	0.1155 \pm 0.0014			12.4 \pm 4.9	110.4 \pm 4.7	2794 \pm 85
A1,BLISS*f(t)	1st Order + Ellipse	0.1164 \pm 0.0014	0.147 \pm 0.013	1.26 \pm 0.12	21.8 \pm 2.7	2826 \pm 93	870 \pm 130
A2,PLD	1st Order	0.11327 \pm 0.00068			13.6 \pm 3.8	2814 \pm 50	2696 \pm 87
A2,PLD	2nd Order	0.11274 \pm 0.00075			11.6 \pm 4.0	256 \pm 15	1757 \pm 95
A2,PLD	1st Order + Ellipse	0.11313 \pm 0.00067	0.1195 \pm 0.0055	1.056 \pm 0.058	11.9 \pm 3.9	2792 \pm 53	1640 \pm 120
A3,BLISS	1st Order	0.1169 \pm 0.0011			15.7 \pm 4.0	2633 \pm 48	1666 \pm 90
A3,BLISS	2nd Order	0.1167 \pm 0.0012			9.0 \pm 5.0	112.0 \pm 9.9	1620 \pm 110
A3,BLISS	1st Order + Ellipse	0.1173 \pm 0.0012	0.95 \pm 0.12	8.1 \pm 1.8	8.9 \pm 7.2	2696 \pm 87	1790 \pm 100

[†]These are derived quantities and are not fitted directly.

[‡]These quantities have been corrected for dilution from WASP-12BC (see supplementary text).

^a ΔBIC is defined from the preferred model from each analysis pipeline.

Supplementary Table 6: Best-fit 4.5 μm Phase Curve Parameters from 2010. A1, A2, and A3 refer to the independent Analyses 1–3.

Detector Model	Astrophysical Model	C_1	D_1	C_2	D_2	F_{day}/F_* [‡] (ppm)	σ_F [‡] (ppm)	χ^2	ΔBIC^a
A1,Poly2	1st Order	0.444 \pm 0.023	-0.165 \pm 0.020			5410 \pm 170	1581 \pm 38	891.63	180
A1,Poly2	2nd Order	0.481 \pm 0.012	-0.150 \pm 0.022	-0.258 \pm 0.031	0.031 \pm 0.017	4380 \pm 180	1485 \pm 35	891.74	81
A1,Poly2	1st Order + Ellipse	0.409 \pm 0.022	-0.099 \pm 0.017			3940 \pm 270	1518 \pm 36	894.4	117
A1,Poly3	1st Order	0.443 \pm 0.027	-0.166 \pm 0.028			5420 \pm 180	1577 \pm 37	888.79	200
A1,Poly3	2nd Order	0.470 \pm 0.018	-0.207 \pm 0.035	-0.281 \pm 0.033	0.020 \pm 0.019	4280 \pm 190	1480 \pm 36	885.72	96
A1,Poly3	1st Order + Ellipse	0.378 \pm 0.028	-0.120 \pm 0.022			3930 \pm 270	1512 \pm 36	892.02	134
A1,Poly4	1st Order	0.445 \pm 0.029	-0.166 \pm 0.035			5400 \pm 170	1574 \pm 37	884.83	227
A1,Poly4	2nd Order	0.387 \pm 0.047	-0.061 \pm 0.046	-0.328 \pm 0.037	0.036 \pm 0.019	4240 \pm 190	1462 \pm 35	881.29	104
A1,Poly4	1st Order + Ellipse	0.253 \pm 0.035	-0.010 \pm 0.027			3740 \pm 260	1482 \pm 36	885.06	125
A1,Poly5	1st Order	0.415 \pm 0.040	-0.228 \pm 0.046			5210 \pm 190	1564 \pm 39	876.41	252
A1,Poly5	2nd Order	0.394 \pm 0.052	-0.061 \pm 0.055	-0.325 \pm 0.037	0.038 \pm 0.019	4220 \pm 210	1459 \pm 36	876.54	141
A1,Poly5	1st Order + Ellipse	0.254 \pm 0.040	-0.011 \pm 0.032			3730 \pm 260	1482 \pm 34	878.21	164
A1,BLISS	1st Order	0.384 \pm 0.037	-0.336 \pm 0.046			4800 \pm 190	1500 \pm 35	898.23	56
A1,BLISS	2nd Order	0.414 \pm 0.044	-0.218 \pm 0.054	-0.265 \pm 0.037	0.031 \pm 0.025	4200 \pm 200	1444 \pm 34	897.25	0
A1,BLISS	1st Order + Ellipse	0.301 \pm 0.038	-0.106 \pm 0.040			3940 \pm 250	1467 \pm 34	897.38	21
A2,PLD	1st Order	0.479 \pm 0.015	-0.135 \pm 0.017			5170 \pm 130	1240 \pm 30	860.05	149
A2,PLD	2nd Order	0.489 \pm 0.016	-0.080 \pm 0.020	-0.252 \pm 0.019	0.042 \pm 0.014	4360 \pm 140	1134 \pm 27	860.09	0
A2,PLD	1st Order + Ellipse	0.437 \pm 0.031	-0.062 \pm 0.016			3740 \pm 210	1167 \pm 28	860.01	46
A3,BLISS	1st Order	0.406 \pm 0.024	-0.190 \pm 0.026			5160 \pm 150	9120 \pm 100	55965	95
A3,BLISS	2nd Order	0.476 \pm 0.030	-0.137 \pm 0.030	-0.263 \pm 0.027	0.043 \pm 0.017	4380 \pm 170	9130 \pm 100	55807	0
A3,BLISS	1st Order + Ellipse	0.365 \pm 0.022	-0.069 \pm 0.020			3940 \pm 210	9130 \pm 100	55844	50

[†]These are derived quantities and are not fitted directly.

[‡]These quantities have been corrected for dilution from WASP-12BC (see supplementary text).

^a ΔBIC is defined from the preferred model from each analysis pipeline.

Supplementary Table 7: Best-fit $4.5\text{ }\mu\text{m}$ Phase Curve Parameters from 2013. A1, A2, and A3 refer to the independent Analyses 1–3.

Detector Model	Astrophysical Model	C_1	D_1	C_2	D_2	F_{day}/F_* \dagger (ppm)	σ_F \ddagger (ppm)	χ^2	$\Delta\text{BIC}^{\dagger a}$
A1,Poly2	1st Order	0.250 ± 0.031	0.035 ± 0.028			4950 ± 180	1613 ± 39	899.32	223
A1,Poly2	2nd Order	0.317 ± 0.041	-0.136 ± 0.041	-0.370 ± 0.045	0.133 ± 0.029	3730 ± 200	1492 ± 36	897.58	93
A1,Poly2	1st Order + Ellipse	0.314 ± 0.029	-0.025 ± 0.022			3080 ± 290	1512 ± 36	911.73	125
A1,Poly3	1st Order	0.267 ± 0.036	0.067 ± 0.030			4940 ± 180	1583 ± 38	895.72	213
A1,Poly3	2nd Order	0.312 ± 0.049	-0.104 ± 0.041	-0.336 ± 0.043	0.144 ± 0.029	3830 ± 200	1472 ± 35	895.32	93
A1,Poly3	1st Order + Ellipse	0.337 ± 0.032	0.007 ± 0.023			3180 ± 290	1495 ± 35	906.96	126
A1,Poly4	1st Order	0.228 ± 0.038	0.088 ± 0.032			4920 ± 190	1567 ± 38	891.32	224
A1,Poly4	2nd Order	0.304 ± 0.050	-0.097 ± 0.047	-0.330 ± 0.045	0.139 ± 0.032	3880 ± 210	1475 ± 33	888.38	124
A1,Poly4	1st Order + Ellipse	0.317 ± 0.036	0.015 ± 0.026			3300 ± 300	1489 ± 34	892.09	138
A1,Poly5	1st Order	0.190 ± 0.040	0.080 ± 0.031			4840 ± 190	1537 ± 35	887.39	231
A1,Poly5	2nd Order	0.254 ± 0.054	-0.097 ± 0.046	-0.299 ± 0.043	0.138 ± 0.032	3910 ± 200	1461 ± 34	885.64	150
A1,Poly5	1st Order + Ellipse	0.291 ± 0.036	0.016 ± 0.025			3430 ± 290	1476 ± 36	890.63	167
A1,BLISS	1st Order	0.182 ± 0.040	0.076 ± 0.031			4890 ± 180	1509 ± 35	908.0	75
A1,BLISS	2nd Order	0.271 ± 0.053	-0.096 ± 0.046	-0.303 ± 0.043	0.122 ± 0.034	3920 ± 210	1440 ± 34	905.23	0
A1,BLISS	1st Order + Ellipse	0.293 ± 0.038	0.018 ± 0.025			3490 ± 280	1449 ± 34	908.11	8
A2,PLD	1st Order	0.276 ± 0.028	-0.063 ± 0.019			4940 ± 150	1275 ± 31	867.11	163
A2,PLD	2nd Order	0.395 ± 0.036	-0.136 ± 0.025	-0.307 ± 0.023	0.034 ± 0.021	3920 ± 150	1158 ± 28	867.01	0
A2,PLD	1st Order + Ellipse	0.348 ± 0.028	-0.058 ± 0.015			3370 ± 220	1164 ± 28	867.04	4
A3,BLISS	1st Order	0.269 ± 0.021	0.004 ± 0.017			5290 ± 140	8657 ± 97	57185	148
A3,BLISS	2nd Order	0.376 ± 0.030	-0.091 ± 0.027	-0.292 ± 0.029	0.041 ± 0.020	4120 ± 160	8658 ± 97	56998	0
A3,BLISS	1st Order + Ellipse	0.317 ± 0.023	-0.038 ± 0.018			3610 ± 210	8657 ± 97	57010	6

\dagger These are derived quantities and are not fitted directly.

\ddagger These quantities have been corrected for dilution from WASP-12BC (see supplementary text).

a ΔBIC is defined from the preferred model from each analysis pipeline.

Supplementary Table 8: Best-fit 4.5 μm Planetary Parameters from 2010. A1, A2, and A3 refer to the independent Analyses 1–3.

Detector Model	Astrophysical Model	Phase Offset (degrees)			$T_{b,\text{day}}^{\dagger}$	$T_{b,\text{night}}^{\dagger}$	$\Delta\text{BIC}^{\dagger a}$
		R_p/R_*	$R_{p,2}/R_*$	$R_{p,2}/R_p$			
A1,Poly2	1st Order	0.1140 ± 0.0012			-20.4 ± 2.2	3143 ± 79	1130 ± 160
A1,Poly2	2nd Order	0.1090 ± 0.0012			-17.5 ± 2.5	2918 ± 81	810 ± 120
A1,Poly2	1st Order + Ellipse	0.1122 ± 0.0011	0.20 ± 0.015	1.79 ± 0.15	-13.5 ± 2.2	2650 ± 110	1210 ± 110
A1,Poly3	1st Order	0.1141 ± 0.0012			-20.7 ± 3.4	3142 ± 81	1140 ± 190
A1,Poly3	2nd Order	0.1084 ± 0.0013			-24.0 ± 3.8	2894 ± 86	900 ± 150
A1,Poly3	1st Order + Ellipse	0.1118 ± 0.0012	0.201 ± 0.015	1.80 ± 0.15	-17.5 ± 3.4	2650 ± 100	1360 ± 130
A1,Poly4	1st Order	0.1142 ± 0.0012			-20.7 ± 4.1	3132 ± 76	1120 ± 200
A1,Poly4	2nd Order	0.1081 ± 0.0013			-8.8 ± 6.5	2888 ± 84	1390 ± 230
A1,Poly4	1st Order + Ellipse	0.1082 ± 0.0014			-2.3 ± 6.1	2678 ± 95	1840 ± 140
A1,Poly5	1st Order	0.1137 ± 0.0013			-29.0 ± 5.6	3078 ± 85	1300 ± 230
A1,Poly5	2nd Order	0.1079 ± 0.0013			-8.8 ± 7.7	2888 ± 89	1360 ± 260
A1,Poly5	1st Order + Ellipse	0.1081 ± 0.0014	0.214 ± 0.015	1.98 ± 0.15	-2.7 ± 7.2	2675 ± 97	1840 ± 160
A1,BLISS	1st Order	0.1121 ± 0.0012			-41.3 ± 4.9	2979 ± 84	1430 ± 180
A1,BLISS	2nd Order	0.1078 ± 0.0013			-27.9 ± 6.1	93.4 ± 2.7	2879 ± 91
A1,BLISS	1st Order + Ellipse	0.1090 ± 0.0014	0.187 ± 0.014	1.71 ± 0.14	-19.6 ± 6.8	2737 ± 96	1250 ± 240
A2,PLD	1st Order	0.11042 ± 0.00084			-15.9 ± 2.0	3174 ± 59	880 ± 150
A2,PLD	2nd Order	0.10656 ± 0.00085			-9.5 ± 2.3	2992 ± 63	780 ± 150
A2,PLD	1st Order + Ellipse	0.10913 ± 0.00081	0.203 ± 0.014	1.86 ± 0.14	-8.3 ± 1.9	2656 ± 91	1070 ± 170
A3,BLISS	1st Order	0.1124 ± 0.0013			-25.1 ± 3.2	3111 ± 75	1360 ± 140
A3,BLISS	2nd Order	0.1075 ± 0.0014			-16.0 ± 3.5	94.6 ± 1.9	330 ± 200
A3,BLISS	1st Order + Ellipse	0.1102 ± 0.0013	1.92 ± 0.12	17.4 ± 1.2	-10.6 ± 3.1	2703 ± 95	1434 ± 99

[†]These are derived quantities and are not fitted directly.

[‡]These quantities have been corrected for dilution from WASP-12BC (see supplementary text).

^a ΔBIC is defined from the preferred model from each analysis pipeline.

Supplementary Table 9: Best-fit 4.5 μm Planetary Parameters from 2013. A1, A2, and A3 refer to the independent Analyses 1–3.

Detector Model	Astrophysical Model	Phase Offset (degrees)			$T_{b,\text{night}}^{\dagger}$	$T_{b,\text{day}}^{\dagger}$	$\Delta\text{BIC}^{\dagger a}$
		R_p/R_*	$R_{p,2}/R_*^{\ddagger}$	$R_{p,2}/R_p$			
A1,Poly2	1st Order	0.1145 \pm 0.0015			8.1 \pm 5.9	295.8 \pm 85	2010 \pm 110
A1,Poly2	2nd Order	0.1102 \pm 0.0015			-23.2 \pm 7.6	261.9 \pm 86	1580 \pm 150
A1,Poly2	1st Order + Ellipse	0.1108 \pm 0.0013	0.252 \pm 0.027	2.27 \pm 0.27	-4.5 \pm 4.3	2340 \pm 120	1460 \pm 120
A1,Poly3	1st Order	0.1141 \pm 0.0015			13.9 \pm 5.2	296.7 \pm 85	1950 \pm 140
A1,Poly3	2nd Order	0.1107 \pm 0.0014			-18.6 \pm 8.5	101.6 \pm 2.5	2644 \pm 86
A1,Poly3	1st Order + Ellipse	0.1112 \pm 0.0013	0.244 \pm 0.026	2.20 \pm 0.26	1.3 \pm 4.0	2370 \pm 120	1400 \pm 130
A1,Poly4	1st Order	0.1136 \pm 0.0014			21.1 \pm 6.1	2975 \pm 84	2120 \pm 140
A1,Poly4	2nd Order	0.1106 \pm 0.0015			-17.8 \pm 9.5	101.4 \pm 2.7	2668 \pm 89
A1,Poly4	1st Order + Ellipse	0.1082 \pm 0.0016	0.225 \pm 0.022	2.08 \pm 0.23	2.7 \pm 4.5	2490 \pm 110	1530 \pm 150
A1,Poly5	1st Order	0.1119 \pm 0.0016			23.2 \pm 7.2	3002 \pm 90	2280 \pm 150
A1,Poly5	2nd Order	0.1110 \pm 0.0015			-21 \pm 12	102.4 \pm 3.0	2692 \pm 88
A1,Poly5	1st Order + Ellipse	0.1075 \pm 0.0015	0.208 \pm 0.020	1.94 \pm 0.21	3.1 \pm 4.9	2570 \pm 110	1650 \pm 150
A1,BLISS	1st Order	0.1109 \pm 0.0016			22.5 \pm 7.6	3056 \pm 92	2350 \pm 150
A1,BLISS	2nd Order	0.1092 \pm 0.0016			-19 \pm 11	100.9 \pm 3.1	2722 \pm 92
A1,BLISS	1st Order + Ellipse	0.1086 \pm 0.0015	0.207 \pm 0.020	1.91 \pm 0.21	3.4 \pm 4.9	2560 \pm 120	1640 \pm 160
A2,PLD	1st Order	0.11094 \pm 0.00091			-13.1 \pm 4.1	3075 \pm 66	1960 \pm 120
A2,PLD	2nd Order	0.1049 \pm 0.0010			-19.1 \pm 3.9	93.2 \pm 1.9	2859 \pm 77
A2,PLD	1st Order + Ellipse	0.10653 \pm 0.00085	0.217 \pm 0.017	2.04 \pm 0.17	-9.6 \pm 2.5	2561 \pm 91	1450 \pm 120
A3,BLISS	1st Order	0.1141 \pm 0.0013			0.8 \pm 3.7	3096 \pm 64	2004 \pm 97
A3,BLISS	2nd Order	0.1104 \pm 0.0014			-13.6 \pm 4.0	94.0 \pm 1.9	1410 \pm 130
A3,BLISS	1st Order + Ellipse	0.1115 \pm 0.0013	2.01 \pm 0.13	18.0 \pm 1.2	-6.9 \pm 3.3	2527 \pm 87	1540 \pm 88

\dagger These are derived quantities and are not fitted directly.

\ddagger These quantities have been corrected for dilution from WASP-12BC (see supplementary text).

a ΔBIC is defined from the preferred model from each analysis pipeline.

This paper has been typeset from a TEX/LATEX file prepared by the author.